ARTICLES
https://doi.org/10.1038/s41477-018-0157-2
nature plants

Translational control of phloem development by RNA G-quadruplex–JULGI determines plant sink strength

Hyunwoo Cho[1,7,8], Hyun Seob Cho[1,8], Hoyoung Nam[2], Hunho Jo[3], Joonseon Yoon[4], Chanyoung Park[1], Tuong Vi T. Dang[1], Eunah Kim[1,2], Jongmin Jeong[1], Soyoung Park[1], Eva-Sophie Wallner[5], Hyungjun Youn[3], Jongmin Park[1], Jinseong Jeon[1], Hojin Ryu[6], Thomas Greb[5], Kyuha Choi[1], Yoontae Lee[1,2], Sung Key Jang[1,2], Changill Ban[3] and Ildoo Hwang[1*]

The emergence of a plant vascular system was a prerequisite for the colonization of land; however, it is unclear how the photosynthate transporting system was established during plant evolution. Here, we identify a novel translational regulatory module for phloem development involving the zinc-finger protein JULGI (JUL) and its targets, the 5′ untranslated regions (UTRs) of the *SUPPRESSOR OF MAX2 1-LIKE4/5* (*SMXL4/5*) mRNAs, which is exclusively conserved in vascular plants. JUL directly binds and induces an RNA G-quadruplex in the 5′ UTR of *SMXL4/5*, which are key promoters of phloem differentiation. We show that RNA G-quadruplex formation suppresses *SMXL4/5* translation and restricts phloem differentiation. In turn, *JUL* deficiency promotes phloem formation and strikingly increases sink strength per seed. We propose that the translational regulation by the JUL/5′ UTR G-quadruplex module is a major determinant of phloem establishment, thereby determining carbon allocation to sink tissues, and that this mechanism was a key invention during the emergence of vascular plants.

Phloem, a living conduit in vascular plants, conducts products of photosynthesis, organic compounds and diverse signalling molecules, which play fundamental roles in plant growth and development[1–3]. The establishment of the phloem system, comprising living conducting cells (sieve elements) and companion cells, was a landmark morphological change underlying the emergence of vascular plants. This important transition in plants enabled the colonization of land and thereby created the terrestrial biosphere, one of the largest evolutionary events in the history of life[2,4,5]. Phloem also serves as a plant-wide communication network integrating cellular energy status and developmental information to orchestrate continuous post-embryonic vegetative and reproductive organ growth. Therefore, phloem differentiation in post-embryonic development should be controlled to optimize symplastic connections based on source supply (via exporters of photosynthates) and sink demand (via importers of fixed carbon)[3]. This has a crucial impact on carbon allocation, and is directly related to crop productivity.

Phloem differentiation accompanies non-reversible cellular reprogramming from meristematic cells called (pro)cambium. In this transition, selective elimination of subcellular organelles, including the nucleus, cell wall remodelling and cytosolic dilution occur through the coordinated regulation of membrane-initiated signalling to transcriptional cascades[1,2,6–8]. After the fate of phloem cells is determined, phloem initial cells are enucleated to develop sieve elements, which are joined together to form a sieve tube. As the cells subsequently lose transcriptional ability, post-transcriptional regulatory processes might be also necessary to establish phloem networks in the plant. However, the post-transcriptional regulatory machinery underlying phloem differentiation is unknown, and its impact on shaping source–sink relationships remains to be elucidated.

In mammalian systems, the dynamics of mRNA and protein signatures have revealed the significance of post-transcriptional regulation for cellular differentiation[9–12], which is mainly governed by RNA-binding proteins (RBPs) and their recognition of specific *cis*-elements in mRNAs. RBPs that specifically recognize and/or modify the primary sequences or secondary structures of genetically encoded RNA are central modulators of mRNA processing during cellular differentiation[13–17]; however, the effects of RBP on the folding status of mRNAs, their specificity and their contribution to post-transcriptional regulation are largely unknown. Given the enucleated condition of phloem cells, RBP-directed mRNA processing would be a central mechanism in post-transcriptional regulation during phloem differentiation, which provides the plasticity of carbon allocation throughout post-embryonic growth.

In this study, we elucidate an evolutionarily conserved mechanism underlying post-transcriptional regulation of phloem differentiation. We identified an uncharacterized zinc-finger (ZnF) RBP, JUL, that specifically binds to consecutive repeats of guanines, folds and stabilizes an RNA G-quadruplex. JUL directs the translational suppression of *SUPPRESSOR OF MAX2 1-LIKE4/5* (*SMXL4/5*), which are central regulators of phloem formation, via G-quadruplex formation of the 5′ UTR, thus restricting phloem differentiation. *JUL* deficiency strikingly enhanced phloem cell number and sink

[1]Department of Life Sciences, POSTECH Biotech Center, Pohang University of Science and Technology, Pohang, Korea. [2]Division of Integrative Bioscience and Biotechnology, Pohang University of Science and Technology, Pohang, Korea. [3]Department of Chemistry, Pohang University of Science and Technology, Pohang, Korea. [4]Crop Seed Development Team, Seed Business Division, FarmHannong Co. Ltd., Daejeon, Korea. [5]Centre for Organismal Studies, Heidelberg University, Heidelberg, Germany. [6]Department of Biology, Chungbuk National University, Cheongju, Korea. [7]Present address: Centre for Organismal Studies, Heidelberg University, Heidelberg, Germany. [8]These authors contributed equally: Hyunwoo Cho, Hyun Seob Cho. *e-mail: ihwang@postech.ac.kr

strength per seed. Based on these findings and a database analysis of JUL and the SMXL family in the green lineage from algae to land plants, we propose that gene-specific translational regulation by the JUL/5′ UTR G-quadruplex module was as a key invention during the emergence of vascular plants.

Results

Identification of JULGI as a negative regulator of phloem differentiation in vascular plants. To investigate the underlying mechanism of phloem establishment during the evolution of vascular plants, we performed a comparative transcriptome analysis of the phloem–cambium region of the woody plant poplar (*Populus tremula*)[18], the herbaceous plant *Arabidopsis thaliana*[19] and sucrose-regulated genes in *Arabidopsis*[20]. In this analysis, we hypothesized that the photosynthetic product sugar controls phloem differentiation, thereby optimizing carbon partitioning throughout the plant body. Interestingly, the expression of two sugar-regulated genes, *At3g15680* and *At2g28790*, overlapped with that of both *Arabidopsis* and poplar phloem–cambium-expressed genes (Fig. 1a). We then performed virus-induced gene silencing (VIGS)[21] in *Nicotiana benthamiana* (tobacco) to examine the functionality of these two candidates and of an additional 24 genes selected through computational and literature analysis as putative vascular regulators and controls. Silencing of tobacco homologues of the well-known vascular regulators *ALTERED PHLOEM DEVELOPMENT* (*NbAPL*) and *WUSCHEL RELATED HOMEOBOX 4* (*NbWOX4*)[2,6] using VIGS resulted in a phenotype in the stem similar to their knockout phenotypes in *Arabidopsis* (Supplementary Fig. 1a). Among those genes, the silencing of a tobacco gene *Niben101Scf0620g02009* (*At3g15680* orthologue), which encodes a plant-specific protein with three RanBP2-type ZnF domains, strikingly increased the population of phloem cells and the expression of the phloem marker gene *APL*, but not markers of the cambium (*WOX4*) or xylem (*XYLEM CYSTEINE PEPTIDASE 2*, *XCP2*)[6] (Fig. 1b and Supplementary Fig. 1b). We named this novel regulator *NbJULGI* (*NbJUL*), which means 'plant shoot' or 'stream' in Korean.

To determine the role of JUL during the evolution of vascular plants, we searched for homologues of tobacco JUL in 23 sequenced species, including chlorophytes, charophytes, bryophytes, lycophytes, monocots and eudicots. We identified homologues in 15 vascular and four non-vascular plant species (Fig. 1c and Supplementary Table 1). However, phylogenetic analysis showed that the four homologues in non-vascular plants are branched in the outgroup of vascular JUL homologues, which implies that the non-vascular JUL homologues are an ancient form of tracheophytic JUL proteins (Fig. 1c and Supplementary Fig. 1d). Thus, the diversification of JUL proteins coincided with the evolution of vascular plants, and the more modern form is present in both early vascular plants, such as *Selaginella* and flowering plants (Fig. 1c), suggesting that JUL played a central role in the emergence of plant vasculature, particularly the phloem. Indeed, silencing of *JUL1* homologues in *Solanum lycopersicum* (tomato) and *Orzya sativa* (rice) also increased the population of phloem cells, which supported an evolutionary conserved role of JUL (Supplementary Fig. 2).

To gain further insights into the functional conservation of JUL in phloem formation, we investigated the effect of the loss of *JUL1* (*At3g15680*) and *JUL2* (*At5g25490*) function in *Arabidopsis*. Single *JUL* mutants exhibited slight aberrations in phloem cell population (Supplementary Fig. 3a), but the combined suppression of both *JUL1* and *JUL2* resulted in increased phloem differentiation compared with the wild type. However, the combined suppression did not affect xylem or vascular cambium development or the expression of related marker genes (Fig. 1d and Supplementary Figs. 1c and 3b). By contrast, overexpression of either *JUL1-HA* or *JUL2-HA* caused severe abnormalities in the phloem, xylem and cambium cell population in stems (Fig. 1d and Supplementary Fig. 3c). We then evaluated the role of JUL in establishing the vascular lineage using the Vascular cell Induction culture System Using *Arabidopsis* Leaves (VISUAL)[22], which synchronizes vascular cell differentiation to enable the quantification of the differentiation efficiency. Silencing both *JUL1* and *JUL2* strongly induced the expression of phloem marker genes such as *SIEVE ELEMENT OCCLUSION-RELATED 1* (*SEOR1*)[23] during the first day of VISUAL induction but did not significantly affect the expression of either the cambium *TDIF RECEPTOR* (*TDR*)- or xylem *IRREGULAR XYLEM 3* (*IRX3*)-associated genes[2]. By contrast, *JUL1* overexpression suppressed the induction of the phloem marker gene *SEOR1* and xylem marker gene *IRX3* on day 3 (Fig. 1e). Thus, we concluded that JUL is evolutionary conserved negative regulator of phloem differentiation in vascular plants.

JUL targets the G-quadruplex motif, exclusively conserved in vascular plants, in the 5′ UTR of *SMXL4/5*. JUL1 and JUL2 have three RanBP2-type ZnF domains, each of which has a conserved arginine residue (R20, R80 and R146 in ZnF1, ZnF2 and ZnF3, respectively) that is required for RNA binding[24,25] (Fig. 2a and Supplementary Fig. 4a). To test if the ZnF domains in JUL1 are necessary for phloem differentiation, we ectopically expressed four *JUL1* arginine-to-alanine mutants, $JUL1^{R20A}$, $JUL1^{R80A}$, $JUL1^{R146A}$ and $JUL1^{R20/80/146A}$. As observed for the *JUL1* and *JUL2* RNAi lines, all of the resulting plants had significant increases in the phloem cell population and phloem marker gene expression (Fig. 2a and Supplementary Fig. 4b). These results indicated that the ZnF domain mutants function as dominant-negative forms of JUL1, potentially interfering the association of wild-type JULs with interacting proteins, and that the RNA-binding activity of JUL1 is essential for its suppression of phloem development.

We then explored whether JUL1 possesses a general RNA-binding capacity or sequence specificity using a random pentaprobe (PP) ssRNA library comprising 1,024 penta-nucleotides diversity[26]. Glutathione S-transferase (GST)-fused JUL1 and its ZnF domain mutants were subjected to an RNA electrophoretic mobility shift assay (EMSA) with the in vitro transcribed PP sets. Only a subset of PPs bound to JUL1, and mutations of JUL1 ZnF domains ($JUL1^{R20/80A}$, $JUL1^{R80/146A}$, $JUL1^{R20/146A}$ and $JUL1^{R20/80/146A}$) completely abolished the mobility shifts of the PPs (Supplementary Fig. 4c), suggesting that JUL1 could have sequence specificity for its target RNAs. To identify the RNA target sequences recognized by JUL1, we performed a systematic evolution of ligands by exponential enrichment (SELEX)[27,28] using a random 30-nucleotide RNA library. We selectively enriched and sequenced the RNA probes bound to JUL1 up to 15 rounds. Interestingly, JUL1-bound RNAs contained G-rich sequences, most of which potentially form G-quadruplexes (57 out of 61 RNAs have a high G-score (>20); Supplementary Fig. 4d), a secondary structure assembled from Hoogsteen-bonded G-quartet stacks[29]. To identify the in vivo mRNA targets of JUL1, we analysed a set of 67 phloem-specific genes with a putative RNA G-quadruplex-forming motif[22,30]. The 5′ UTR of *SMXL5*, a key positive regulator of phloem differentiation in *Arabidopsis*[31], was shown to have the highest possibility of G-quadruplex formation determined by computational scoring algorithm (G-score) based on the number of G-tetrads and the length of loops connecting G-tetrads[32] (Fig. 2b and Supplementary Table 2).

A phylogenetic analysis of the SMXL family showed that SMXL3/4/5 are exclusively found in vascular plants and grouped separately from the other SMXLs, which are found in all plant species (Fig. 2c, Supplementary Table 3). The SMXL5 homologue in *S. moellendorffii*, an ancient vascular plant, is monophyletic but outgrouped with SMXL3/4/5, implying that SmSMXL is an ancestor of SMXL3/4/5. Interestingly, a G-quadruplex-forming sequence is found in the 5′ UTR of 23 out of 24 SMXL4/5 homologues and SmSMXL, but other SMXLs from 23 sequenced plant species

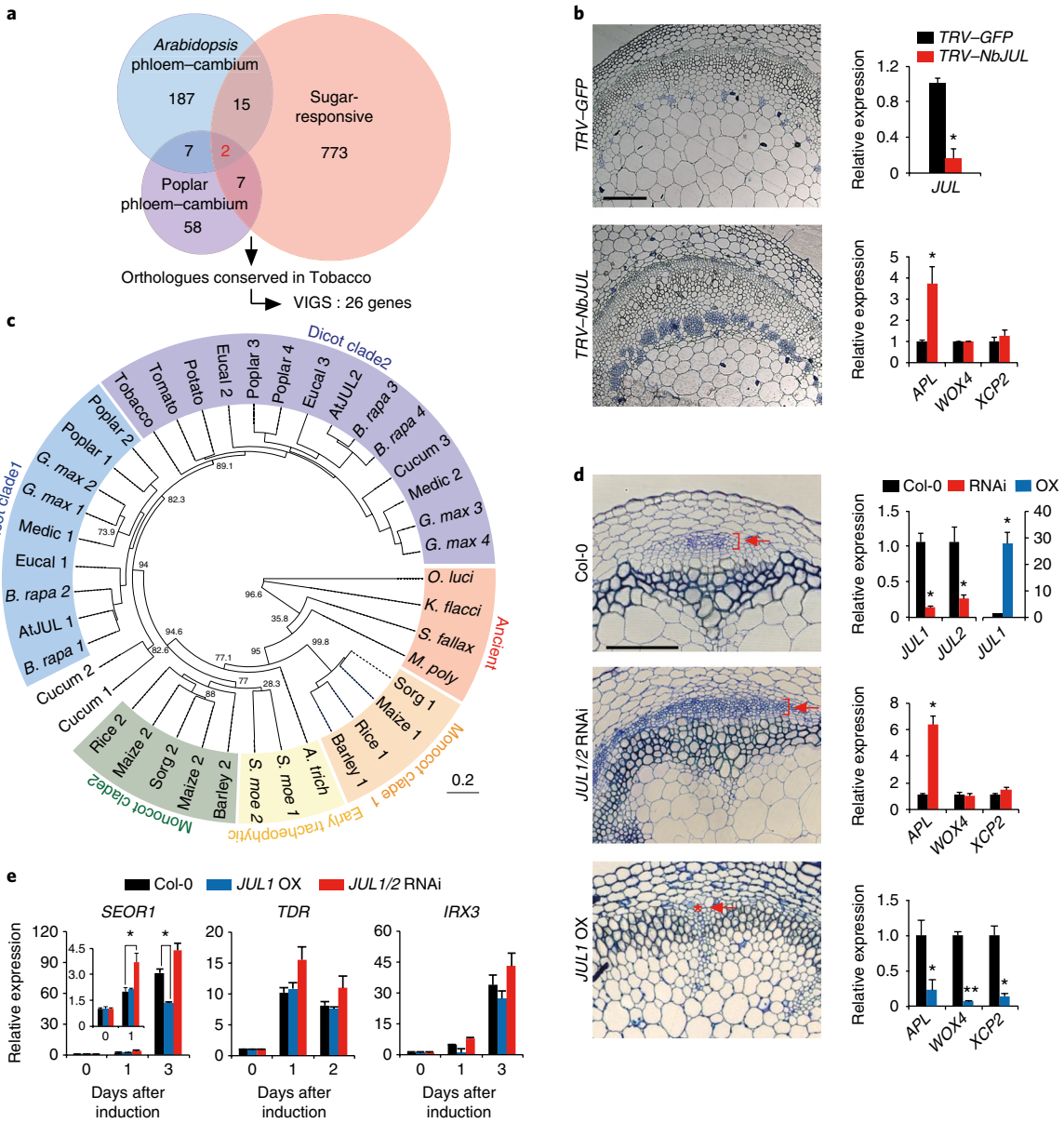

Fig. 1 | Identification of a negative regulator, JULGI, in phloem differentiation. a, Potential regulators of phloem differentiation selected by a comparative analysis among poplar and *Arabidopsis* cambium- and phloem-specific transcriptomes and sugar-responsive genes. Orthologues of the selected genes were then silenced in *N. benthamiana* using VIGS to assess their function. **b**, Representative stem cross-section of *NbJUL*-silenced plants (*TRV–NbJUL*) and the negative control, *TRV–GFP*, at 4 weeks after infiltration (left panels). Scale bars, 100 μm. Expression of *NbJUL* and vascular cell markers (*NbAPL* for phloem; *NbWOX4* for cambium; *NbXCP2* for xylem) (right panels). Phloem cells are marked with blue. These experiments were repeated three times independently with similar results. Data are shown as mean ± s.e.m. ($n = 3$; $^*P < 0.05$ by the two-tailed Student's *t*-test). **c**, Maximum likelihood (ML) phylogenetic analysis of JUL proteins found in the green lineage. NbJUL homologues of 19 species among 23 species with sequenced genomes are shown. ML bootstrap values are shown in branch points of each group, and grouping was based on taxon classification and homology with NbJUL. The scale bar indicates evolutionary distances in substitutions per amino acid. **d**, Representative stem cross-sections of wild-type (Col-0), *JUL1/2*-silenced (*JUL1/2* RNAi) and *35S:JUL1-HA Arabidopsis* (*JUL1* OX; left panels). Scale bars, 100 μm. Expression of *JUL1*, *JUL2* and relative marker genes are shown (*APL* for phloem; *WOX4* for cambium; *XCP2* for xylem) (right panels). Red arrows indicate phloem cell layers. These experiments were repeated three times independently with similar results. Data are shown as mean ± s.e.m. ($n = 3$; $^*P < 0.05$, $^{**}P < 0.01$ by the two-tailed Student's *t*-test). **e**, qRT–PCR analysis of *JUL1/2* RNAi and *JUL1* OX showing relative expression of vascular cell markers in VISUAL at designated time points (*SEOR1* for phloem; *TDR* for cambium; *IRX3* for xylem). These experiments were repeated three times independently with similar results. Data are shown as mean ± s.e.m. ($n = 3$; $^*P < 0.05$ by the two-tailed Student's *t*-test). See also Supplementary Figs. 1–3, and Supplementary Table 1.

have few G-quadruplex-forming motif in the 5′ UTR (Fig. 2c and Supplementary Table 3). Therefore, the G-quadruplex-forming motif in the *SMXL4/5* 5′ UTR, which was exclusively conserved in vascular plants, probably serves as a specific substrate of JUL proteins for phloem development. We thus examined the phenotypes of *smxl4/5* loss-of-function mutants in tobacco and *Arabidopsis*[31]. Silencing of *SMXL5* in tobacco resulted in a dramatic decrease in phloem differentiation (Fig. 3a). Interestingly, compared with fully differentiated phloem of the wild-type vasculature, *smxl4/5* *Arabidopsis* mutant had larger but undifferentiated sieve elements

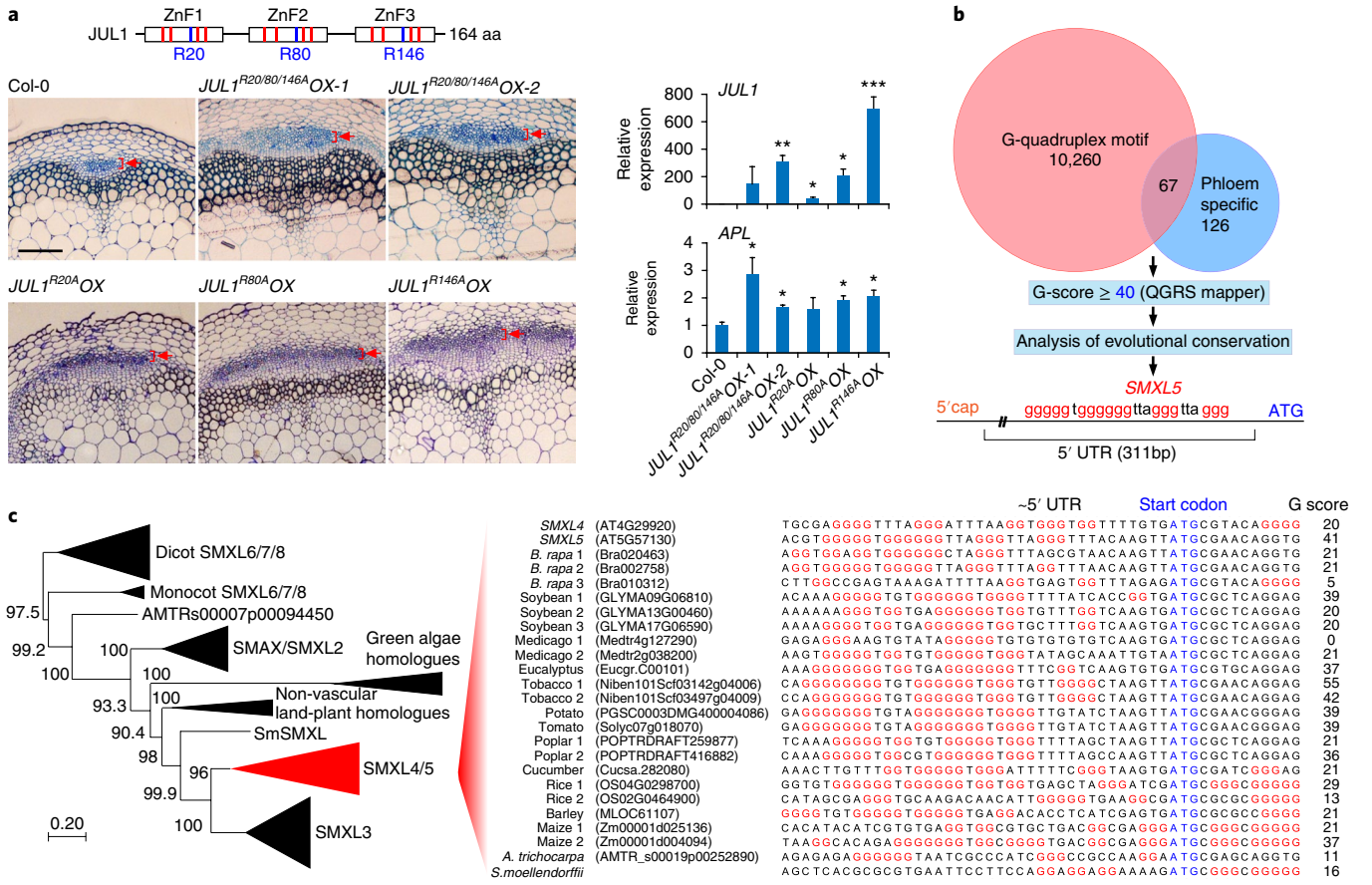

Fig. 2 | JUL1 targets the G-quadruplex-forming sequence in the *SMXL5* 5′ UTR that is exclusively conserved in vascular plants. a, Diagram of triple RanBP2-type ZnF domains of JUL1 (top). Representative stem cross-sections of *JUL1* OX harbouring mutations on the ZnFs (R20A, R80A, R146A, R20/80/146A) (left panels). Red arrows indicate phloem. Scale bars, 100 μm. The relative expression of *JUL1* and the phloem marker gene (*APL*) are shown (right panels). These experiments were repeated three times independently with similar results. Data are shown as mean ± s.e.m. ($n = 3$; $^{*}P < 0.05$, $^{**}P < 0.01$, $^{***}P < 0.001$ by the two-tailed Student's *t*-test). **b**, Identification of JUL1-targeted RNAs in phloem differentiation. Among the 67 phloem-specific transcripts with putative G-quadruplex-forming motifs, the evolutionally conserved target in vascular plants with the highest probability (G-score) of G-quadruplex formation was selected (*SMXL5*). Red characters indicate the putative G-quadruplex-forming motif of its 5′ UTR. **c**, ML phylogenetic analysis of SMXL proteins and the 5′ UTR sequences in SMXL5 homologue proteins of 23 species with sequenced genomes. Monophyletic subclades were condensed arbitrarily based on homology with AtSMXLs and taxon classification. ML bootstrap values are shown on branch points of each wedge (left). The G-quadruplex-forming motifs (red) 38 nt upstream and 10 nt downstream of the start codon are shown (right). G-quadruplex-forming motifs in the 5′ UTR of SMXL5 homologues were conserved exclusively in vascular plants. G-scores are shown for each *SMXL5* 5′ UTR. The scale bar indicates evolutionary distances in substitutions per amino acid. See also Supplementary Fig. 4 and Supplementary Tables 2 and 3.

that still contained a nucleus and chloroplasts and displayed significantly reduced levels of phloem marker gene expression[31] (Fig. 3b,c). These results collectively suggest that *SMXL4/5* 5′ UTRs are conserved target of JUL for the emergence of phloem during land plant evolution.

JUL directly binds to the RNA G-quadruplex motif in the *SMXL5* 5′ UTR and induces G-quadruplex formation. To test if JUL proteins directly bind to the single-stranded mRNA or the RNA G-quadruplex of *SMXL5*, we performed an EMSA using the GST–JUL1 and GST–JUL2 proteins in the presence or absence of potassium, which is required for the formation of the G-quadruplex. Both JUL1 and JUL2 retarded the mobility of the G-quadruplex-forming motif in the *SMXL4* and *5* 5′ UTR probe or *telomeric repeat-containing RNA* (*TERRA*) used as a positive control compared to the GST control; however, *mSMXL5* 5′ UTR(1), *mSMXL5* 5′ UTR(3), a mutated single-stranded RNA, or JUL1 arginine-to-alanine mutants ($JUL1^{R20A}$, $JUL1^{R80A}$, $JUL1^{R146A}$, $JUL1^{R20/80A}$, $JUL1^{R20/146A}$, $JUL1^{R80/146A}$ and $JUL1^{R20/80/146A}$) lost the JUL1-induced mobility shift (Fig. 4a and Supplementary Fig. 5a–e). *mSMXL5* 5′ UTR(2), a mutated variant that produces just two layers of the G-quartet, bound to JUL proteins less efficiently than did the *SMXL5* 5′ UTR (Fig. 4a and Supplementary Fig. 5a). The dissociation constant (K_d) of this binding was estimated to be 130 nM in the absence of potassium and 230 nM in the presence of potassium, implying that JUL1 preferentially binds to the primary *SMXL5* 5′ UTR sequence (Fig. 4b). Next, we visualized the interaction between the *SMXL5* 5′ UTR G-quadruplex and JUL1 proteins using a surface binding system, which condenses RNA probes at the liquid-solid interface of a protein-coated bead surface with either strong G-quadruplex stabilizing potassium or weak sodium or non-G-quadruplex stabilizing lithium. Cy5-labelled RNA probes were subjected to glutathione-sepharose beads coated with GST–JUL1, and the resulting G-quadruplex formed on the bead surface was simultaneously visualized using Cy5 and the G-quadruplex sensor, Thioflavin T (ThT)[33,34] (Fig. 4c). The fluorescence signal emitted by ThT completely overlapped with the JUL1-coated bead surface in the presence of potassium but was reduced in the presence of sodium or lithium, whereas the Cy5 signal that overlapped with the bead surface was increased by sodium or lithium (Fig. 4c). JUL1 arginine mutations

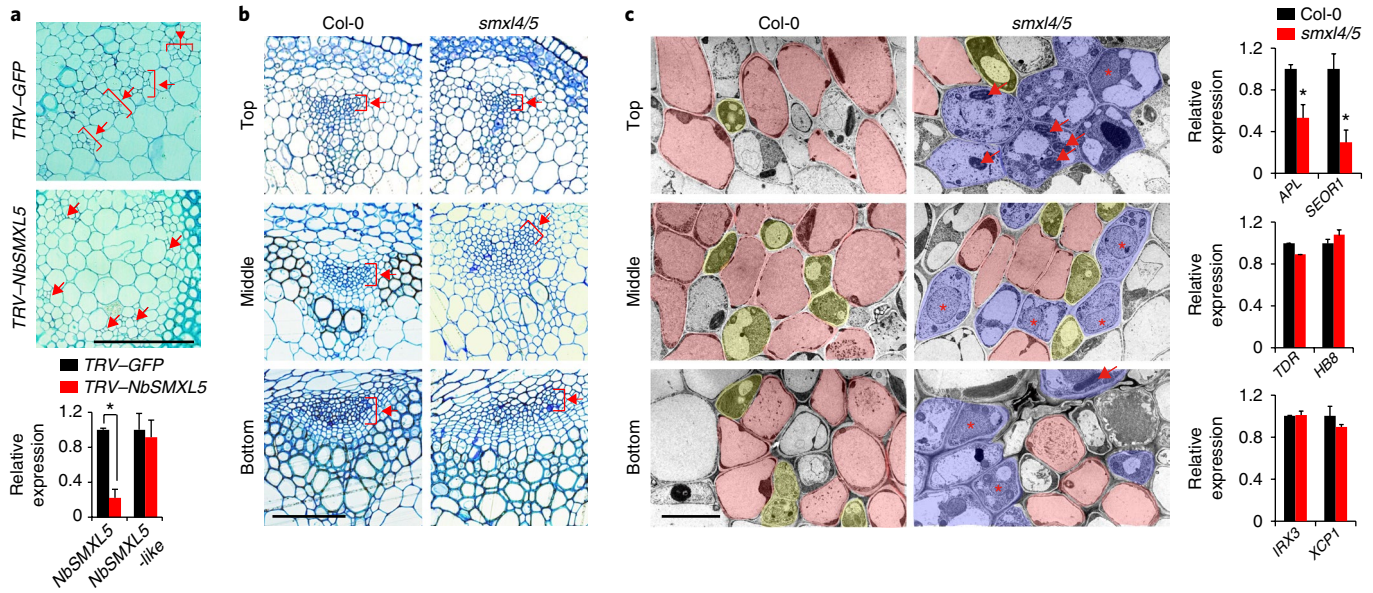

Fig. 3 | Phenotypes of smxl4/5 loss-of-function mutants. a, Representative stem cross-section of *NbSMXL5*-silenced tobacco plants (top). *TRV–GFP* was the negative control. Red arrows indicate phloem. Scale bar, 100 µm. Relative expression of *NbSMXL5* and *NbSMXL5*-like in *TRV–GFP* and *TRV–NbSMXL5* lines (bottom). These experiments were repeated at least three times independently with similar results. Data are shown as mean ± s.e.m. ($n = 3$; $^*P < 0.05$ by the two-tailed Student's *t*-test). **b**, Representative cross-sections of wild-type (Col-0) and *smxl4/5 Arabidopsis* stems. Red arrows indicate phloem. Scale bar, 100 µm. **c**, Representative transmission electron microscopy (TEM) images of wild-type (Col-0) and *smxl4/5 Arabidopsis* phloem regions showing undifferentiated phloem cells in *smxl4/5*. Red and yellow indicate sieve elements and companion cells, respectively. Blue indicates undifferentiated phloem cells (left panels). Red arrows indicate chloroplasts and red asterisks indicate nuclei. Scale bar, 5 µm. Relative expression of vascular marker genes in *smxl4/5* (*APL*, *SEOR1* for phloem; *TDR, HB8* for cambium; *IRX3, XCP1* for xylem) (right panels). These experiments were repeated three times independently with similar results. Data are shown as mean ± s.e.m. ($n = 3$; $^*P < 0.05$ by the two-tailed Student's *t*-test).

compromised the overlapping fluorescence at the bead surface (Supplementary Fig. 6a). These data suggest that the direct binding of JUL1 to the G-quadruplex of the *SMXL5* 5′ UTR occurs at the RanBP2-type ZnF. This notion was verified using another specific G-quartet-sensing fluorescence probe, N-methylmesoporphyrin IX (NMM)[35] (Supplementary Fig. 6b). In addition, JUL1 bound to both the full-length *SMXL5* 5′ UTR and to 5′ UTR fragments containing the G-quadruplex (Supplementary Fig. 6c). To further confirm the formation of RNA G-quadruplex, we examined the structure of 63 bases *SMXL5* 5′ UTR containing U-rich region by a reverse transcriptase stalling-based method[36] (Fig. 4d). The reverse transcriptase was stalled on the well-characterized RNA G-quadruplex in *NRAS* 5′ UTR used as a positive control in the presence of potassium or pyridostatin (PDS), a strong G-quadruplex stabilizing ligand[37] (Supplementary Fig. 6d). Reverse transcriptase stalling occurred on *SMXL5* 5′ UTR, but not *mSMXL5* 5′ UTR(1) and *mSMXL5* 5′ UTR(3) (Fig. 4d and Supplementary Fig. 6d). This stalling was observed in the presence of potassium, but not lithium. Moreover, PDS strongly increased the stalling even in the presence of lithium. These data suggested that RNA G-quadruplex is formed in 5′ UTR of *SMXL5* rather than G–U paired hairpin structure (Fig. 4d and Supplementary Fig. 6d).

We then measured the circular dichroism (CD) absorptivity of the G-quadruplex-forming motif in *SMXL5*. The molar ellipticity of the G-rich motif exhibited a negative peak at 240 nm and a positive peak at 264 nm (Fig. 4e), which is a signature spectrum of the RNA G-quadruplex[29]. Interestingly, incubation of JUL1 with the unstructured *SMXL5* 5′ UTR increased the peak at 264 nm, suggesting that JUL1-induced folding of the G-quadruplex via its direct binding to the *SMXL5* 5′ UTR (Fig. 4e). Moreover, incubating JUL1 with folded *SMXL5* 5′ UTR increased the peak at 264 nm (Fig. 4e), indicating that the binding of JUL1 increases the formation of the folded *SMXL5* 5′ UTR. Thus, JUL1 primarily recognizes the single-stranded G-quadruplex-forming motif and potentially functions as an inducer of RNA G-quadruplex formation. We confirmed the binding of JUL1 to the *SMXL5* 5′ UTR in vivo using RNA-immunoprecipitation in protoplasts, revealing that the *SMXL5* 5′ UTR, but not the *mSMXL5* 5′ UTR(1), co-immunoprecipitated with haemagglutinin (HA)-tagged JUL1 (Fig. 4f). Collectively, these results suggest that JUL functions in G-quadruplex folding through direct interaction, particularly in the 5′ UTR of *SMXL5*.

To investigate JUL action on *SMXL5*, we assessed spatial patterning of *JUL* and *SMXL5* expression in the vascular tissue of the inflorescence stem using β-glucuronidase (GUS) and yellow fluorescence protein (YFP) under the control of the *JUL1* promoter and *SMXL5* promoter, respectively. Both *JUL1* and *SMXL5* were expressed specifically in phloem and cambium regions of *Arabidopsis* inflorescence stems (Fig. 5a,b), supporting the notion that *JUL1* functions together with *SMXL5* during phloem development. Interestingly, *JUL1* was also expressed in pollens, and vascular bundles of root, cotyledon, and funicle (Supplementary Fig. 7). Next, to test whether JUL associated with the G-quadruplex within the *SMXL5* 5′ UTR, we traced the cellular distribution of JUL1 and the *SMXL5* 5′ UTR using a MS2 hairpin/MS2 coat protein-based RNA monitoring system[38] in *Arabidopsis* protoplasts. The *SMXL5* 5′ UTR conjugated to the 24xMS2 binding hairpin structure was directly visualized by GFP-tagged MS2 coat proteins. *SMXL5* 5′ UTR transcripts were co-localized with JUL1 in the *Arabidopsis* protoplasts, but *mSMXL5* 5′ UTR(1) and JUL1 (RA) did not co-localize with JUL1 and *SMXL5* 5′ UTR, respectively (Fig. 5c), indicating that JUL1 associates with the G-quadruplex motif of the *SMXL5* 5′ UTR in vivo. To gain further insight into the cellular function of JUL1 during phloem differentiation, we examined transgenic lines that overexpress *JUL1* fused to a nuclear localization sequence (NLS) or a nuclear export

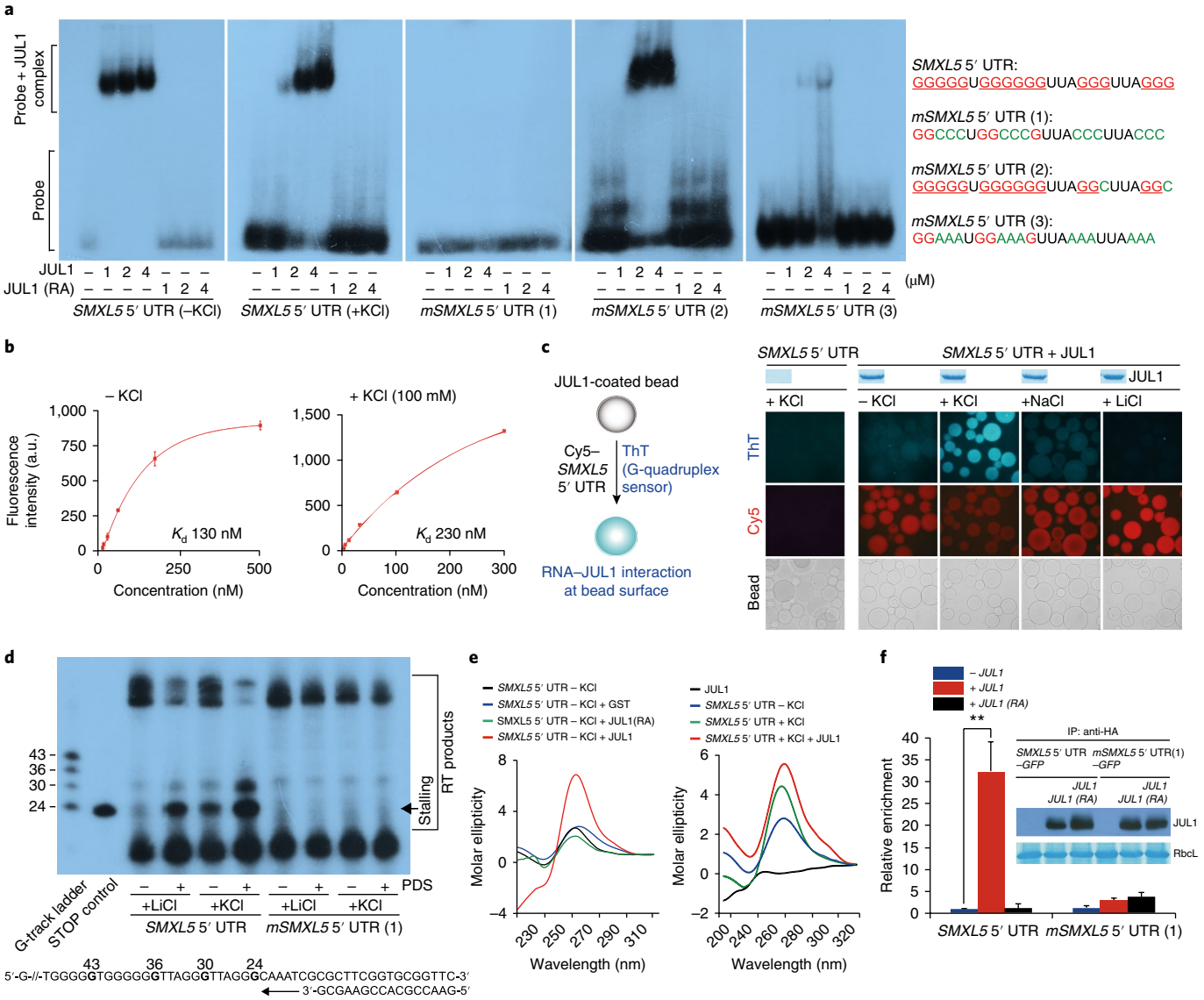

Fig. 4 | JUL1 directly binds to the G-quadruplex-forming motif and induces G-quadruplex formation of the *SMXL5* 5′ UTR. a, RNA EMSA of the *SMXL5* 5′ UTR and its variant probes with GST-fused JUL1 (JUL1) or GST-JUL1$^{R20/80/146A}$ (JUL1 (RA)) in the absence or presence of KCl. GST was used as a negative control. *SMXL5* 5′ UTR forms a G-quadruplex with three-layered G-quartets in the presence of KCl; *mSMXL5* 5′ UTR(1) has an unstructured form (G to C substitution); *mSMXL5* 5′ UTR(2) forms a G-quadruplex with two-layered G-quartets; *mSMXL5* 5′ UTR(3) has an unstructured form (G to A substitution). The sequences of the *SMXL5* 5′ UTR variants are presented (right). **b**, The binding affinity between JUL1 and the *SMXL5* 5′ UTR in the absence or presence of potassium. Data are shown as mean ± s.e.m. ($n = 2$). **c**, Scheme for detecting interaction of the G-quadruplex and JUL1 using an RNA probe (Cy5) and G-quartet sensor (ThT) (left). ThT and Cy5 fluorescence at the surface of JUL1-coated beads with *SMXL5* 5′ UTR in the presence of K^+, Na^+ or Li^+. JUL1 protein bound in beads was visualized by Coomassie-blue staining (right). **d**, RT-stop assay of *SMXL5* 5′ UTR RNA G-quadruplex structure. The in vitro transcripts including 63 bp of *SMXL5* 5′ UTR or *mSMXL5* 5′ UTR(1) were used as a template for RT-stop assay. G-track ladder represents the size of RT products and the first G position of each G track in template. **e**, Circular dichroism (CD) spectra showing the increased formation of parallel G-quadruplexes involving the unstructured *SMXL5* 5′ UTR in the presence of JUL1 but not in GST or JUL1 (RA) in the absence of K^+ (left). CD spectra showing an increase in the formation of G-quadruplexes from the folded *SMXL5* 5′ UTR in the presence of JUL1 and K^+ (right). **f**, Native RNA-immunoprecipitation assay indicating the association of JUL1 with the *SMXL5* 5′ UTR but not JUL1 (RA) or *mSMXL5* 5′ UTR(1) in *Arabidopsis* protoplasts. JUL1 or JUL1 (RA) was immunoprecipitated with the anti-haemagglutinin (HA) antibody. Rubisco (RBC) was used as a loading control. The *SMXL5* and *mSMXL5* 5′ UTR enrichment values were normalized by the input controls. These experiments were repeated three times independently with similar results. Data are shown as mean ± s.e.m. ($n = 3$, $^{**}P < 0.01$ by the two-tailed Student's *t*-test). See also Supplementary Fig. 5, 6.

sequence (NES). The overexpression of *JUL1-NES* phenocopied the overexpression phenotype of wild-type *JUL1* and suppressed the expression of phloem marker genes, whereas *JUL1-NLS* overexpression increased phloem differentiation and the levels of the corresponding marker genes, similar to *JUL1/2* RNAi and dominant-negative JUL1 ZnF mutant lines (Fig. 5d,e).

JUL-mediated formation of the G-quadruplex inhibits *SMXL5* translation. The 5′ UTR is subject to translational regulation in the cytosol, and the G-quadruplex typically confers a translational suppressor element onto the 5′ UTR[39]. Therefore, we hypothesized that cytosolic JUL1 modulates the expression of its specific target, *SMXL5*, through 5′ UTR G-quadruplex-mediated translational

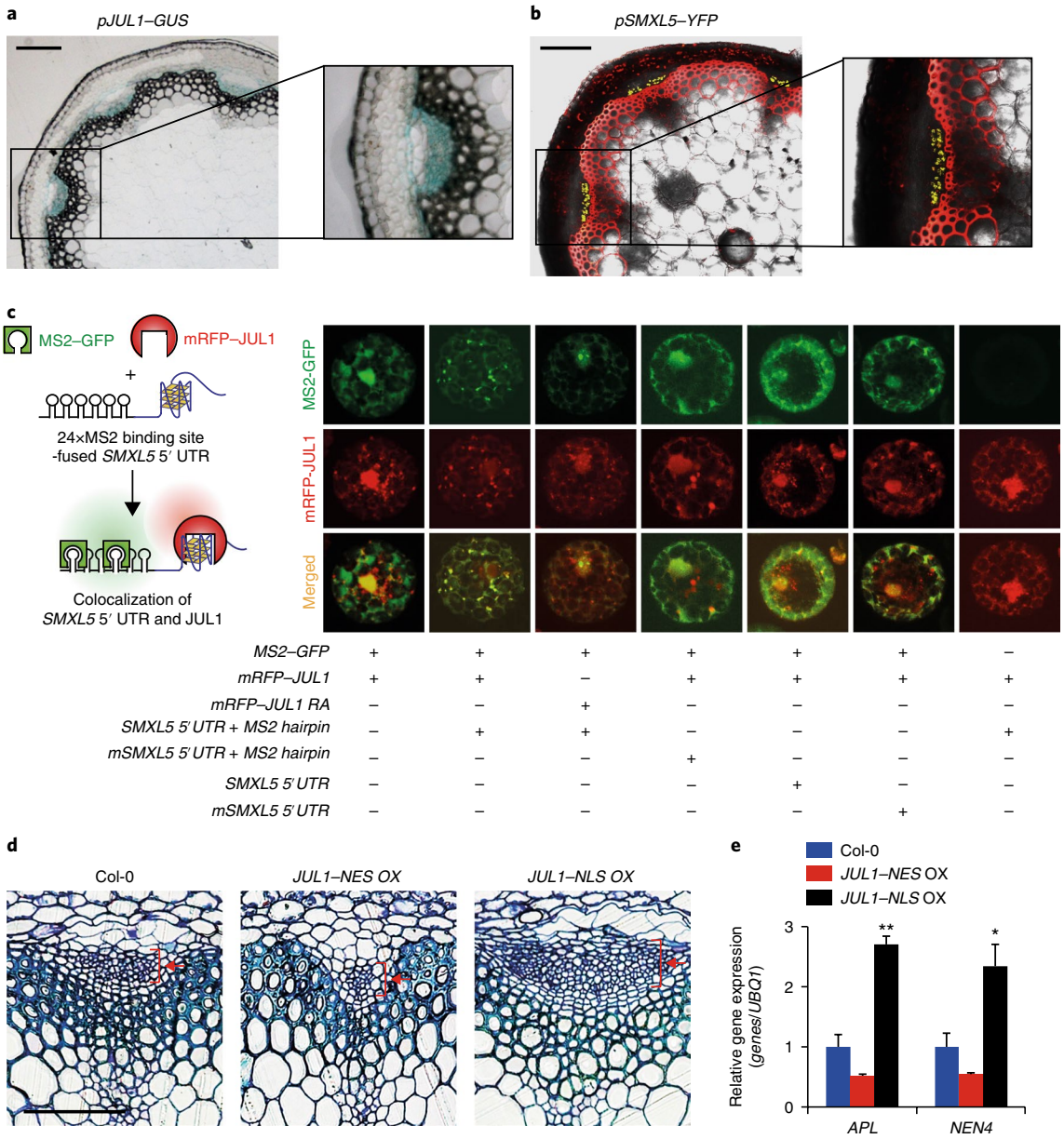

Fig. 5 | Cytosolic JUL and SMXL5 in the phloem and cambium controls phloem development. a, Histochemical detection of *JUL* expression in the phloem and cambium of 6-week-old *Arabidopsis* transgenic stems expressing *pJUL1-GUS*. Scale bars, 100 μm. **b**, Phloem- and cambium-specific *SMXL5* expression in six-week-old *Arabidopsis* stems expressing *pSMXL5-YFP*. Scale bar, 100 μm. **c**, Schematic diagram of MS2/24xMS2 binding site-fused 5′ UTR system for visualizing the *SMXL5* 5′ UTR in *Arabidopsis* protoplasts (left). GFP signals indicate the cellular distributions of the *SMXL5* 5′ UTR or its variants. mRFP signals indicate the cellular distributions of JUL1 or JUL1 (RA). Co-localization of MS2 and JUL1 on the *SMXL5* 5′ UTR is shown in yellow (right panels). **d**, Representative stem cross-sections. Scale bar, 100 μm. **e**, Relative expression levels of phloem markers in the wild-type, *JUL1-NLS* OX and *JUL1-NES* OX plants. These experiments were repeated three times independently with similar results. Data are shown as mean ± s.e.m. ($n = 3$, $^{*}P < 0.05$, $^{**}P < 0.01$ by two-tailed Student's *t*-test). See also Supplementary Fig. 7.

control. To elucidate the mode of JUL1 action on *SMXL5* mRNA, we monitored the ribosomal association of *SMXL5* in protoplasts (Fig. 6a). JUL1 strikingly decreased the polysomal association of the *SMXL5* 5′ UTR-fused *GFP* mRNA but not the *TUB4* mRNA used as a control (Fig. 6a). The *mSMXL5* 5′ UTR(1) mutant compromised the inhibitory effect of JUL1 on the polysomal association of *GFP* mRNA (Supplementary Fig. 8a), indicating that JUL1 suppresses the incorporation of *SMXL5* transcripts to translationally active ribosomes through 5′ UTR G-quadruplex recognition.

We then investigated whether JUL1 binding to the 5′ UTR G-quadruplex affected the translation of *SMXL5* using a GFP reporter assay under the control of the *SMXL5* 5′ UTR or the mutant 5′ UTRs (mSM*XL5* 5′ UTR(1), (3)). The GFP signal under the control of the *SMXL5* 5′ UTR in the protoplasts was reduced by JUL1 or JUL2 in a dose-dependent manner, whereas *mSMXL5* 5′ UTR(1) or (3) completely abolished the suppressive effect of JUL1 (Fig. 6b,c and Supplementary Fig. 8b,d). In line with disruption in the interactions between $JUL1^{R20/80/146A}$ and the G-quadruplex in vitro, $JUL1^{R20/80/146A}$ did not affect the translation of *SMXL5* 5′ UTR-fused *GFP* mRNA; however, neither JUL1 nor the mutation in the *SMXL5* 5′ UTR changed the transcription level of the reporter (Fig. 6b,c). Consistent with these results, the reporter assay using *SMXL4* or *SMXL5* 5′ UTR-fused *luciferase* (*LUC*) showed a JUL1-dependent decrease in reporter activity, whereas the G-quadruplex-disrupting mutations

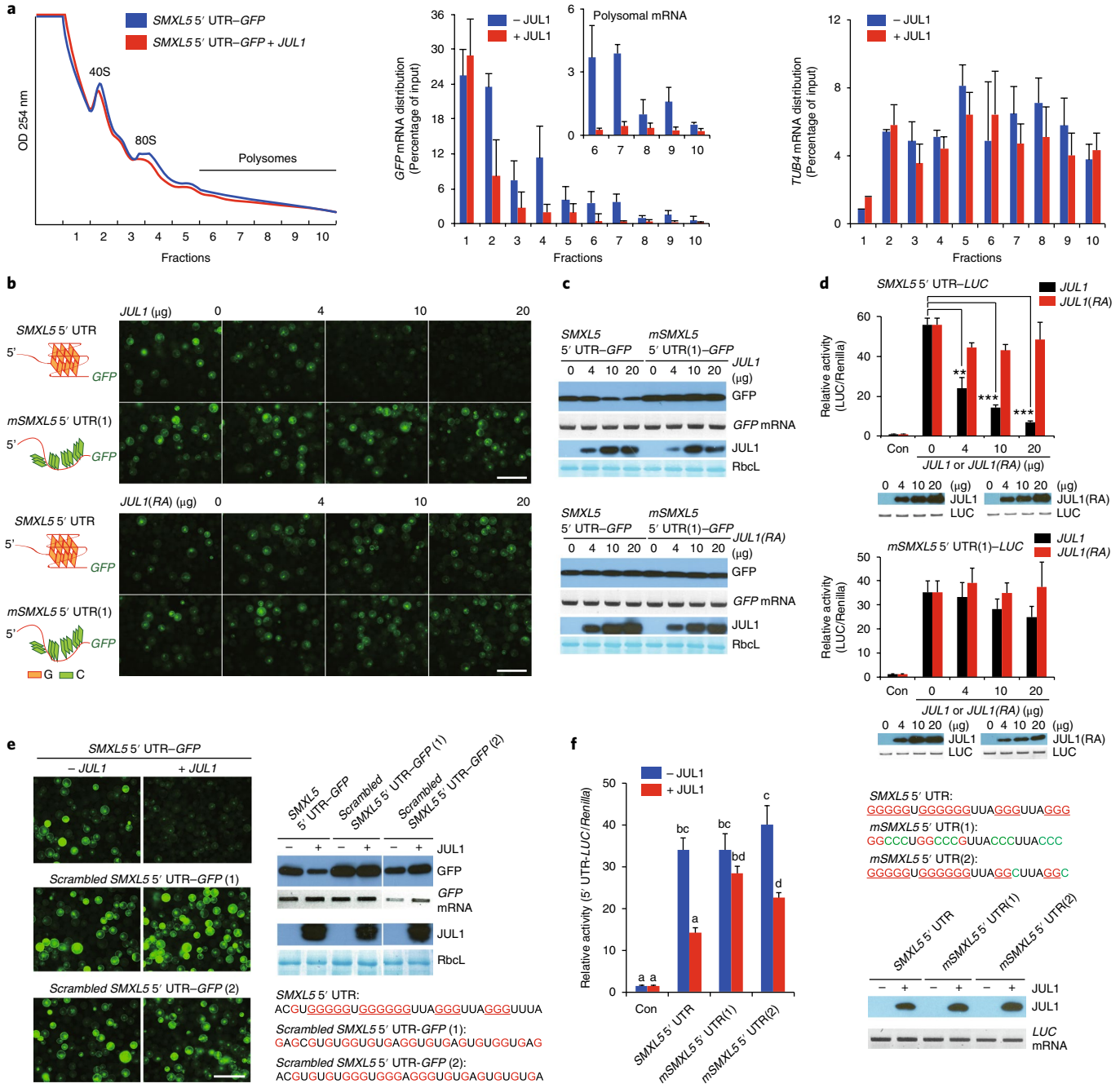

Fig. 6 | JUL1 interaction with the G-quadruplex in the *SMXL5* 5′ UTR is necessary and sufficient for JUL1-mediated translation inhibition of *SMXL5*. **a**, Polysome profiling assays with a sucrose density gradient accompanied by qRT–PCR to monitor the *SMXL5* 5′ UTR–*GFP* transcripts associated with ribosomes in the absence or presence of JUL1. Absorption spectra at 254 nm show the distribution of ribosomes (40 S, 80 S, and polysomes) in each fraction (left). qRT–PCR showing the abundance of the *SMXL5* 5′ UTR–*GFP* and *TUB4* transcripts in each fraction (middle and right). These experiments were repeated three times independently with similar results, and data are shown as mean ± s.e.m. **b**, Representative *Arabidopsis* protoplasts expressing *GFP* under the control of the *SMXL5* 5′ UTR or *mSMXL5* 5′ UTR(1) in a JUL1- or JUL1$^{R20/80/146A}$ (JUL1 (RA))-dose-dependent manner. Scale bars, 200 μm. **c**, *SMXL5* 5′ UTR–GFP and *mSMXL5* 5′ UTR(1)–GFP abundances with increasing concentration of JUL1 (top) or JUL1 (RA) (bottom). JUL and GFP proteins were determined by immunoblot while *GFP* transcripts were assessed using RT–PCR. **d**, Reporter assays using the *SMXL5* 5′ UTR- or *mSMXL5* 5′ UTR(1)-fused *luciferase* (*LUC*) with JUL1 (WT) or JUL1 (RA). LUC activities were normalized using the 35 S promoter-driven Renilla activity. JUL1 and JUL1 (RA) protein levels were determined by immunoblot while *LUC* transcripts were assessed using RT–PCR. These experiments were repeated three times independently with similar results. Data are shown as mean ± s.e.m. ($n = 3$; $^{**}P < 0.01$, $^{***}P < 0.001$ by the two-tailed Student's *t*-test). **e**, Representative *Arabidopsis* protoplasts expressing *GFP* under the control of the *SMXL5* 5′ UTR or *Scrambled SMXL5* 5′ UTRs in a *JUL1*-dependent manner (left panel). Scale bars, 200 μm. GFP abundances in the absence or presence of JUL1 (right panel). JUL1 and GFP proteins were determined by immunoblot, and the *GFP* transcripts were assessed using RT–PCR. The sequences of the *Scrambled SMXL5* 5′ UTRs are presented in the lower panel. Red underlined Gs indicate a G-quadruplex-forming motif. **f**, Luciferase (LUC) reporter assay using the *SMXL5* 5′ UTR and its mutant variants. LUC activities were normalized by Renilla activity. JUL1 proteins and *LUC* transcripts were determined by immunoblot and RT–PCR, respectively. These experiments were repeated three times independently with similar results. Sample means with different letters represent significant differences ($n = 3$; $P < 0.05$ by two-way ANOVA with the post hoc Tukey HSD test). See also Supplementary Fig. 8.

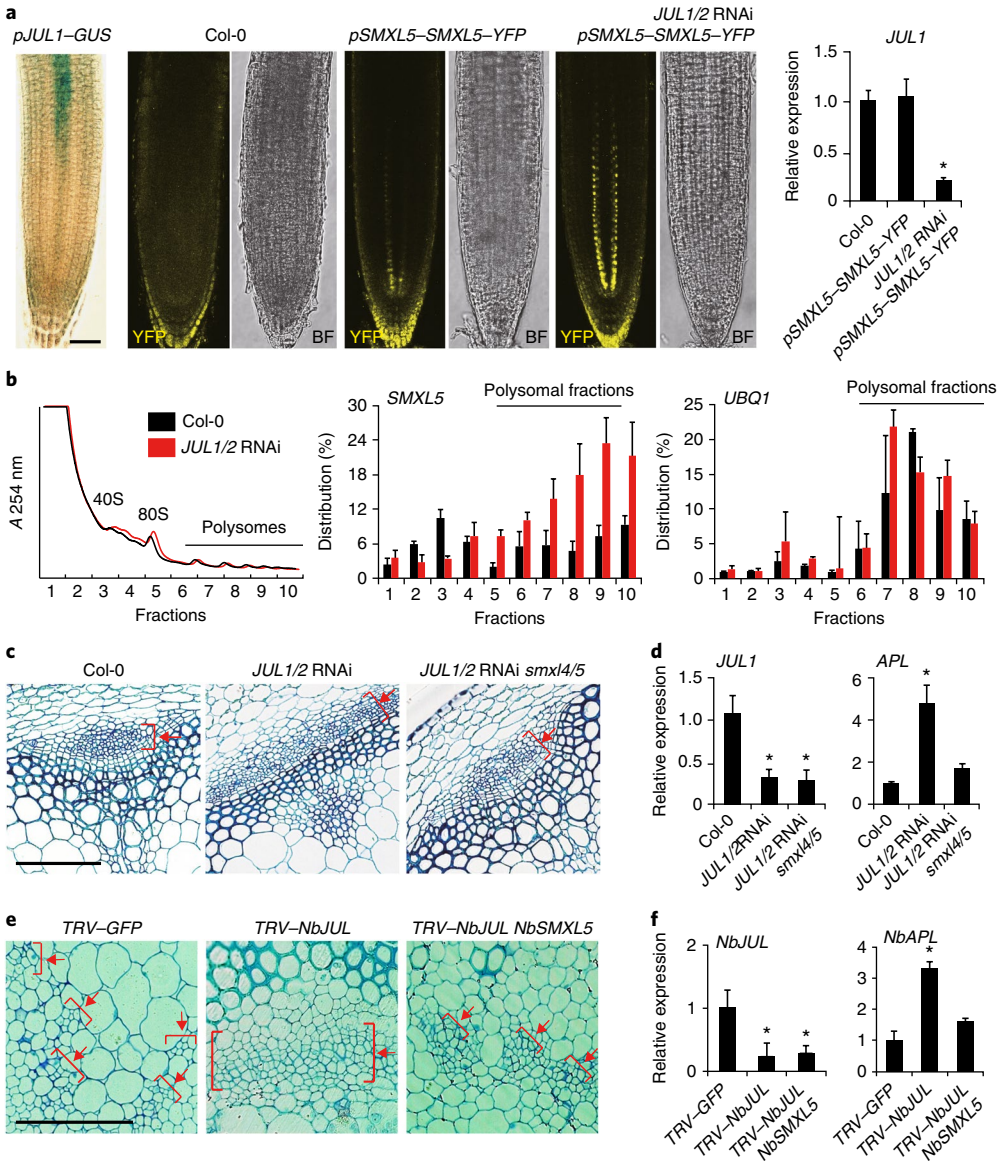

Fig. 7 | JUL-directed *SMXL4/5* translational repression inhibits phloem differentiation. a, SMXL5 protein localization in seven-day-old *pJUL1–GUS*, *pSMXL5–SMXL5–YFP*, and *pSMXL5–SMXL5–YFP JUL1/2* RNAi lines. Histochemical staining of GUS indicates expression of *JUL1* in the maturation and elongation zone. YFP fluorescence indicates SMXL5 localization in the basal part of the meristematic zone in wild type and throughout the meristematic zone in *JUL*-deficient lines (left panels). Scale bar, 50 μm. qRT–PCR analysis showing the expression of *JUL1* in each line (right). These experiments were repeated three times independently with similar results, and data are shown as mean ± s.e.m. ($n = 3$; $^*P < 0.05$ by the two-tailed Student's *t*-test). **b**, Polysome profiling assays with a sucrose density gradient in 7-day-old wild-type and *JUL1/2* RNAi seedlings. Absorption spectra at 254 nm show the distribution of ribosomes (40 S, 80 S and polysomes) in each fraction (left). Abundance of *SMXL5* (middle) and *UBQ1* (right) transcripts are shown in each fraction. These experiments were repeated three times independently with similar results, and data are shown as mean ± s.e.m. **c**, Representative stem cross-sections of wild-type, *JUL1/2* RNAi and *JUL1/2* RNAi in *smxl4/5* plants. Red arrows indicate phloem. Scale bar, 100 μm. **d**, qRT–PCR analysis showing the expression of *JUL* and the phloem marker *APL* in each line from **c**. These experiments were repeated three times independently with similar results. Data are shown as mean ± s.e.m. ($n = 3$; $^*P < 0.05$ by the two-tailed Student's *t*-test). **e**, Representative stem cross-sections of *GFP*-, *NbJUL*-, or *NbJUL*- and *NbSMXL5*-silenced tobacco plants. *TRV–GFP* was used as the negative control. Red arrows indicate phloem. Scale bar, 100 μm. **f**, qRT–PCR analysis showing the expression of *NbJUL* and the phloem marker *NbAPL* in each line. These experiments were repeated three times independently with similar results. Data are shown as mean ± s.e.m. ($n = 3$; $^*P < 0.05$ by the two-tailed Student's *t*-test).

in the *SMXL5* 5′ UTR (*mSMXL5* 5′ UTR(1)) or *JUL1*$^{R20/80/146A}$ expression resulted in failure of effector-dependent translational suppression (Fig. 6d, and Supplementary Fig. 8c). Furthermore, mutations in the *SMXL5* 5′ UTR that disrupt G-quadruplex formation but have the same number of guanines (*Scrambled SMXL5* 5′ UTR(1) and (2)) also abolished JUL1-dependent translational suppression (Fig. 6e). In addition, in the presence of JUL1, the *SMXL5* 5′ UTR mutant with two layers of G-quartet (*mSMXL5* 5′ UTR(2)) had less of an inhibitory effect on the reporter activity than did *SMXL5* 5′ UTR, but its effect was higher than that of the single-stranded *SMXL5* 5′ UTR mutant (*mSMXL5* 5′ UTR(1); Fig. 6f). These data suggest that direct recognition of the RNA G-quadruplex-forming motif and stabilization of the G-quadruplex in the *SMXL5* 5′ UTR leads to the efficient JUL1-dependent suppression of its translation.

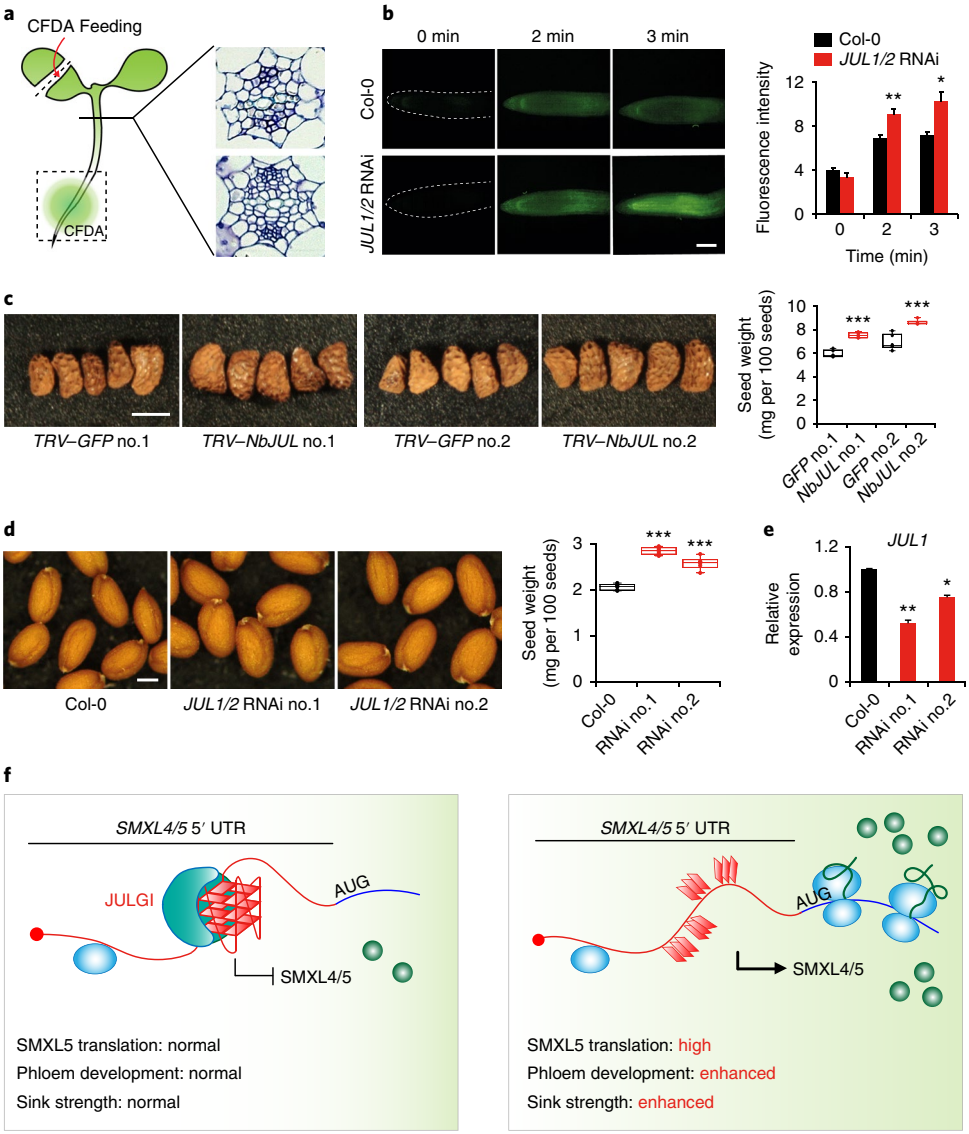

Fig. 8 | *JUL* deficiency enhances sink strengths of seed in tobacco and *Arabidopsis*. **a**, Scheme to trace phloem flow of four-day-old *Arabidopsis* seedlings using CFDA and representative hypocotyl cross-section images of Col-0 and *JUL1/2* RNAi line. **b**, CFDA fluorescence images in the root tip of Col-0 and *JUL1/2* RNAi line at indicated time points and quantification of CFDA fluorescence. These experiments were repeated three times independently with similar results. Data are shown as mean ± s.e.m. ($n = 8$; $^{*}P < 0.05$, $^{**}P < 0.01$ by the two-tailed Student's *t*-test). Scale bar, 100 mm. **c**, Seed size and morphology (left panels). Scale bar, 2 mm. Seed weight of *TRV-GFP* as a control and *TRV-NbJUL* tobacco plants (right). Whiskers extending from the boxes include maximum/minimum value ($n = 6$; $^{***}P < 0.001$ by the two-tailed Student's *t*-test). Dots indicate individual values. **d**, Seed size and morphology (left panels). Scale bar, 200 µm. Seed weight of wild-type and *JUL1/2* RNAi *Arabidopsis* lines (right). These experiments were repeated three times independently with similar results. Whiskers extending from the boxes include maximum/minimum value ($n = 6$; $^{***}P < 0.001$ by two-tailed Student's *t*-test). Dots indicate individual values. **e**, Relative expression of *JUL1* in wild-type and *JUL1/2* RNAi lines assessed by qRT-PCR. These experiments were repeated three times independently with similar results. Data are shown as mean ± s.e.m. ($n = 3$; $^{*}P < 0.05$, $^{**}P < 0.01$ by the two-tailed Student's *t*-test). **f**, Model of JUL action on the G-quadruplex of the *SMXL4/5* 5′ UTR in phloem differentiation, in which *JUL*-mediated G-quadruplex formation restricts phloem development through *SMXL4/5* translational suppression. See also Supplementary Fig. 9.

Remarkably, the *SMXL5* 5′ UTR and its mutant variants did not show any difference in reporter activity in the absence of JUL1 (Fig. 6f). Moreover, the JUL1-mediated inhibitory effect on translation and the insensitivity to JUL1 rendered by the G-quadruplex mutation were recapitulated in HEK293T mammalian cells (Supplementary Fig. 8e). This supports the proposed molecular action of *trans*-acting JUL1 on the G-quadruplex during translation but also indicates the potency of JUL1 as a stabilizer of the G-quadruplex.

JUL negatively regulates *SMXL5* to suppress phloem development. To further decipher the in planta function of JUL-mediated 5′ UTR G-quadruplex formation of *SMXL5* during phloem differentiation, we monitored SMXL5 under the control of the native *SMXL5* promoter in *JUL1/2*-silenced roots. *JUL1* promoter activity was restricted to the elongation and maturation zone of roots, whereas SMXL5 was only detected in phloem initial cells of the basal meristem[31] (Fig. 7a and Supplementary Fig. 7b). However, *JUL1/2*-silencing increased and expanded SMXL5 detection to the distal part of the basal meristem. Furthermore, the suppression of *JUL1/2* dramatically increased the polysomal association of *SMXL5* in plants, supporting the notion that accumulation of SMXL5 resulted from increased translation by silencing of *JUL1/2* (Fig. 7b).

To examine in planta relationships between JUL and SMXL4/5 in phloem differentiation, we observed the effect of defective *SMXL4/5* in the *JUL*-silenced plants. The *smxl4/5* mutation partially restored the phenotype of the *JUL1/2* RNAi lines to wild type (Fig. 7c), as indicated by decreased expression of the phloem marker gene *APL* (Fig. 7d). Suppression of *NbSMXL5* by VIGS also decreased the population of phloem cells in tobacco and partially restored the *NbJUL*-silencing phenotype (Fig. 7e,f). These genetic data support that JUL functions upstream of *SMXL4/5* in phloem development.

JUL controls sink strength per seed in vascular plants. We then tested whether increased number of phloem cells relates to phloem transporting capacity. To trace phloem flow, we monitored the translocation of 5,6-carboxyfluorescein diacetate (CFDA)[40], a phloem symplasmic tracer, from the cotyledon to the root tip (Fig. 8a). *JUL1/2* RNAi increased phloem cells in the hypocotyl and significantly enhanced CFDA accumulation at the root tip compared with Col-0 control (Fig. 8a,b), suggesting the enhanced phloem flow capacity of *JUL1/2* RNAi lines. Next, we examined the phenotype of sink tissues, such as seeds, in *JUL*-deficient tobacco, and *Arabidopsis*. *NbJUL* silencing in tobacco significantly increased the size and weight of seeds by approximately 26–29% compared with the control (Fig. 8c). Consistent with the seed phenotype of *JUL*-deficient tobacco, *JUL1/2* RNAi *Arabidopsis* lines also exhibited increased size and weight of seeds by up to 37% and 22%, respectively, compared to wild-type plants but not the total seed yield (Fig. 8d,f and Supplementary Fig. 9a). However, seed weight of Col-0 plants after pollination with *JUL1/2* RNAi lines (male) was similar to that of self-pollinated Col-0 plants (Supplementary Fig. 9b) and the *JUL1* promoter is not active in embryo and endosperm (Supplementary Fig. 7d). Root weight and the root/shoot ration of RNAi lines was increased compared to control plants (Supplementary Fig. 9c,d). Moreover, the increase in seed size and weight was associated with the degree of *JUL1* silencing in each RNAi line (Fig. 8e), indicating positive correlation between increased number of phloem cells and enhanced sink strength per seed. Collectively, the association between an increase in phloem formation as a consequence of *JUL* deficiency and increased sink strength supports the notion that phloem conducting capacity is directly associated with sink strength (Fig. 8f).

Discussion

In this work, we reveal that (1) a ZnF JULGI, its target *SMXL4/5* 5′ UTR, and RNA G-quadruplex-directed translational regulation of *SMXL4/5* is a central genetic framework of phloem development that is exclusively conserved in vascular plants, and (2) the transporting capacity of phloem networks controls sink strength.

During the diversification and expansion of land plants[4,5], the emergence of vascular systems enabled use of aerial and soil resources in the terrestrial environment for growth and development[2,41]. Dramatic increases in the photosynthetic capacity of land plants placed the photosynthetic product sucrose at the centre of plant growth and development[42]. Regardless of the importance of sucrose as a major product of photosynthesis and energy source in the plant life cycle, it is still unknown whether sucrose functions as an indicator of the cellular energy status during phloem development. Exclusive conservation of JULGI and the *SMXL4/5* 5′ UTR G-quadruplex in vascular plants suggests that the sucrose-inducible JULGI[20] (Fig. 1a) and RNA secondary structure-driven regulation of *SMXL4/5* co-evolved as a core module for phloem emergence during evolution. Interestingly, potassium concentration of phloem exudate in stem near source tissues is higher than other stem regions close to sink tissues in cassava and castor bean[43]. This downward gradient of potassium concentration from the source to the sink might affect the RNA G-quadruplex formation and translation via JUL in the phloem sieve tube network.

The remarkable conservation of the molecular basis of phloem development and the association of conductance capacity with sink strength in plants may be exploited to develop new strategies to enhance crop productivity. It is well known that photosynthetic source activity and sink strength are closely linked to crop yields[44,45]. Substantial efforts to improve crop productivity have focused on overexpression-based genetic manipulation of a specific gene to enhance source or sink activity[46], which mostly exhibits pleiotropic effects and is restricted to few crop species. Combined with genome-editing technology, targeted deletion of the conserved negative regulator *JUL* in phloem development (Supplementary Fig. 2 and Supplementary Table 1) could specifically enhance sugar-conducting activity by increasing phloem cell number and subsequently lead to substantial improvement of biomass production in various crop plants.

Among diverse RNA secondary structures, G-quadruplexes are extensively encoded in all eukaryote genomes such as *Arabidopsis ATM and RAD3-related* (*ATR*)[29,47,48] and appear to be associated with various cancers and neurodegenerative diseases[49–52]; however, in vivo roles of RNA G-quadruplexes and active (un)folding mechanisms of G-quadruplex-forming sequences in biological processes are unclear. In vivo folding analyses demonstrate a global unfolded status of RNA G-quadruplexes in mammalian cells and yeast[53], suggesting that G-rich single-strand RNA-binding proteins may restrain the energetically favourable folding of G-rich elements. However, the folding status of RNA G-quadruplexes could also be influenced (in)directly by their *trans*-acting RBPs, and the equilibrium between unstructured single-strand and structured G-quadruplexes could be modulated transiently in a condition- or cell type-dependent manner, accentuating active roles of *trans*-acting RBPs on the folding status of RNA G-quadruplex in vivo[54]. In this study, we revealed that JUL functioned as a G-quadruplex-folding inducer and/or stabilizer assisted by triple RanBP2-type ZnF via preferential binding affinity to consecutive repeats of guanine. Moreover, we revealed the first example of a functional G-quadruplex contributing to cellular differentiation with a *trans*-acting RBP in planta. Further in vivo analysis and structural analysis of JUL-RNA G-quadruplex complexes would be necessary to elucidate folding dynamics of G-quadruplexes in various differentiation processes.

The 5′ UTR is a key element for translation initiation, which involves recruiting translation initiation factors and ribosomes. The inhibitory effects of an RNA G-quadruplex located in the 5′ UTR have been intuitively explained by the extremely stable structure of the G-quadruplex and the subsequent steric hindrance for scanning ribosomes in mammalian cells[39,55]. In this study, we found that both JUL1 and the G-quadruplex, but not the single-stranded G-rich element, are required for strong translational suppression, suggesting that the translational inhibition is caused by intramolecular JUL1-mediated G-quadruplex formation or G-quadruplex/JUL1 recruiting of an unknown translational suppressor. Interestingly, overexpression of *JUL1* exhibited global but specific effects on the entire vascular network, and the *smxl4/5* mutation partially rescued the *JUL*-silencing phenotype. Since RanBP2-type ZnF proteins can function as splicing regulators in humans[24,25] and *JUL1* is expressed in both phloem and cambium regions, these results indicate that JUL1 could target multiple RNAs in the cambium nucleus as well as *SMXL4/5* in the cytosol, post-transcriptionally modifying its targets to modulate the specification and differentiation of phloem. Indeed, G-quadruplex-forming motifs are located in the exon and intron regions of many phloem-specific transcripts in *Arabidopsis*[22,56], including in the exons of vascular differentiation regulators such as *BARELY ANY MERISTEM 3*[57], *HIGH CAMBIAL ACTIVITY 2*[58], *NEN1*[7], *SEOR2*[23] and *TERRA*[59] (Supplementary Table 2 and Supplementary Fig 5e). JUL-interacting partners and JUL targets in the nucleus as well as cytosol would provide diverse regulatory layers for the post-transcriptional and translational control of plant life cycle.

Although we propose that JUL acts on the genetically encoded G-quadruplex-forming sequence on the 5′ UTR in *SMXL4/5* to specify the vascular cell files, further studies on the post-transcriptional mode of action on other vascular regulators of JUL are necessary to elucidate the full spectrum of post-transcriptional control for establishment of conductive networks in plants. In addition, characterization of conserved negative actions of *JUL* on phloem development in various crop plants and its manipulation will provide not only powerful strategies to maximize sugar partitioning into harvestable sink tissues, but also insights into how plants evolved vascular systems to regulate source–sink relationships.

Methods

Plant materials and growth conditions. *A. thaliana* Col-0 and WS-2 ecotype were used as a wild type and genetic backgrounds for the transgenic lines. All seeds were germinated in media containing 1/2 Gamborg B5 salts (Duchefa), 1% sucrose and 0.8% phytoagar (pH 5.7) under long-day conditions (16 h light/8 h dark) at 24 °C. After a week, the seedlings were transplanted into pots and grown under long-day conditions. The *smxl5, smxl4/5, pSMXL5–YFP, pSMXL5–SMXL5–YFP* and *pSMXL5–SMXL5–YFP* in *smxl4/5* lines were provided by Thomas Greb, Heidelberg University, Germany. *jul1* (FLAG_293A10; 5′ UTR insertion) and *jul2* (GK-268A03-015068; 5′ UTR insertion) were obtained from ABRC. For the protoplast isolation, plants were grown under short-day conditions (10 h light/14 h dark) and fully expanded leaves of 3- to 4-week-old plants were used. *N. benthamiana* seeds were sown and grown in pots under long-day conditions at 26 °C for 5–6 weeks. Tomato plants (*Solanum lycopersicum* cv. Heinz 1706) were grown in pots under long-day conditions at 22 °C for 5–7 weeks.

Plasmid construction and generation of transgenic plants. For the VIGS assay, the fragmented cDNAs of *NbJUL*, *SlJUL* and *NbSMXL5* were cloned into the TRV2 vector. For RNAi constructs, partial sequences of *AtJUL1* (*AT3G15680*) and *AtJUL2* (*AT5G25490*) were amplified and ligated together, then the ligated product was amplified and cloned into a pCR8/GW/TOPO vector (Invitrogen). The cloned cDNA was amplified using the M13 forward and reverse primers, then used for Gateway cloning into pK7GWIWG2(I)[60]. The tissue-specific expression of *AtJUL1* and *AtJUL2* was visualized by amplifying the 1.5-kb sequences upstream of the translation start site from *Arabidopsis* genomic DNA then cloning them into pCXGUS-P[61]. For the protoplast reporter assay, the full-length 5′ UTR of *SMXL5*, and *JUL1* were cloned into plant expression vectors that contained GFP, luciferase and HA[62]. The recombinant proteins were generated and purified by cloning full-length *JUL1* and *JUL2* cDNA into pGEX5-1 (Promega). The point mutations in *JUL1* (*JUL1*^{R20A}, *JUL1*^{R80A}, *JUL1*^{R146A}, *JUL1*$^{R20/80A}$, *JUL1*$^{R20/146A}$, *JUL1*$^{R80/146A}$ and *JUL1*$^{R20/80/146A}$) and *SMXL5* 5′ UTR (*mSMXL5* 5′ UTR(1), *mSMXL5* 5′ UTR(2), or *Scrambled SMXL5* 5′ UTR(1–3)) were generated using the QuickChange Site-Directed Mutagenesis Kit (Stratagene). Transgenic plants were generated by cloning the full-length cDNA sequences of *JUL1, JUL2* and the *JUL1* point-mutant versions into a pCB302ES vector containing the 35S promoter and a HA epitope tag. These constructs were then transformed into *Agrobacterium tumefaciens* GV3101, and the *Arabidopsis* plants were transformed using the floral dipping method[63].

Transient expression in *Arabidopsis* protoplasts. Mesophyll protoplasts and plasmid DNA were prepared as described by previously[62]; then, 2×10^4 protoplasts were transfected with 20 µg of plasmid DNA and incubated for 6 h at room temperature. For the reporter assay, 2×10^4 protoplasts were transfected with 20 µg of total plasmid DNA composed of different combinations of the reporters (*SMXL5* 5′ UTR–*LUC, mSMXL5* 5′ UTR(1)-*LUC, mSMXL5* 5′ UTR(2)-*LUC, SMXL4* 5′ UTR–*LUC SMXL5* 5′ UTR–*GFP, mSMXL5* 5′ UTR(1)–*GFP, mSMXL5* 5′ UTR(2)–*GFP* or *Scrambled SMXL5* 5′ UTR–*GFP*(1–3)), effectors (*JUL1-HA* or *JUL1*$^{R20/80/146A}$*-HA*,) and an internal control (*p35S-Rennila*). For RNA-immunoprecipitation, protoplasts were transfected with 40 µg of total plasmid DNA composed of *SMXL5* 5′ UTR–*GFP*, or *mSMXL5* 5′ UTR(1)–*GFP* were co-transfected into protoplasts with or without *JUL1-HA*. All assays were conducted a minimum of three times and similar results were obtained in all experiments.

Virus-induced gene silencing. *pTRV2*-derived vectors were transformed into the *A. tumefaciens* strain GV2260. *A. tumefaciens* cultures containing *pTRV1* or *pTRV2* constructs were incubated overnight at 28 °C, harvested, and resuspended in 10 mM $MgCl_2$ and 10 mM MES. Virulence was induced by adding 200 µM acetosyringone and incubating for 2–4 h at room temperature. *A. tumefaciens* cells containing *pTRV1* or *pTRV2* were mixed in a 1:1 ratio, and infiltrated into the leaves of three-week-old *N. benthamiana* plants. For VIGS in tomato, the *pTRV2-SlJUL* construct was transformed into the *A. tumefaciens* strain GV3101, then the *Agrobacterium* mixtures containing *pTRV1* and *pTRV2* were infiltrated into the cotyledons of two-week-old tomato plants. Approximately 3–4 weeks after the Agro-inoculation, the plants were used for experiments.

VISUAL analysis. VISUAL was performed as described by previously[22]. RNA from cultured cotyledons was extracted using TRIzol (Thermo Fisher Scientific). Relative gene expression was calculated using three independent quantitative PCR analyses.

Phylogenetic analysis. To search for homologues of JULs and SMXLs in Viridiplantae, we analysed 23 existing taxa with released genome sequences on public databases (EnsemblPlants release 36, Phytozome version 12, Solgenomics version 3.1, and Klebsormidium nitens v1.1). Protein sequences of two JUL proteins and each of eight SMXL proteins in *Arabidopsis* were used as query for tBLASTn search. Sequences of homologues within top 10 hits with e-value $\leq10^{10}$ were subjected to a phylogenomic pipeline. The *Arabidopsis* input sequences were obtained from TAIR10. The top 10 of tBLASTn hits (sorted by e-value) from each query were parsed manually from each taxon to create homologue candidates. Sequence alignments of JULs were built using ClustalO and SMXLs using MAFFT under default settings, respectively[64,65]. Protein sequence alignments were further trimmed by trimAl[66] for more accurate alignment. ML trees were built based on the JTT matrix-based model. Branch supports were estimated using ultrafast bootstrap[67] approximation approach with 1,000 bootstrap replicates (-bb 1000) using IQ-TREE[68]. The best amino acid substitution model for each alignment was selected with the Nearest-Neighbour-Interchange ML heuristic method.
Gene IDs in Fig. 1: Uniprot IDs (*B. rapa* 1; M4CBM4, *B. rapa* 2; M4DX81, *B. rapa* 3; M4D046, *B. rapa* 4; M4DVF8, Eucalyptus 1; A0A059BST6, Eucalyptus 2; A0A059CPS7, Eucalyptus 3; A0A059CSU8, Medicago 1; A0A072UG31, Medicago 2; G7JB51, Soybean 1; C6T4M1, Soybean 2; C6SXC6, Soybean 3; I1K8W8, Soybean 4; I1JUE6, Potato; M1ABJ1, Poplar 1; B9GWD5, Poplar 2; A9PB85, Poplar 3; A9P992, Poplar 4; B9IKV1, Barley 1; F2EG93, Barley 2; F2EDY2, Rice 1; Q9SNS0, Rice 2; Q6Z6E6, Maize 1; A0A1D6NVS8, Maize 2; B4FHT6, Maize 3; C0P4Z1, Sorghum 1; C5Z3T1, *O. lucimarinus*; A4S2N4, *S. moellendorffii* 1; D8ST26, *S. moellendorffii* 2; D8SY24, Cucumber 1; A0A0A0K718, Cucumber 2; A0A0A0KTI0), Phytozome IDs (*M. polymorpha*; Mapoly0019s0131, *S. fallax*; Sphfalx0050s0025, Sorghum 2; Sb04g007110, Cucumber 3; Cucsa.162240), Solgenomics IDs (Tobacco; Niben101Scf01620g02009, Tomato; Solyc08g067180).

Identification of SMXL in *S. moellendorffii*. Specific genomic scaffold region (GL377574:2177376-2180294) was designated as putative ORF of *AtSMXL5* homologue (*SmSMXL*). Based on this sequence, putative *SmSMXL* ORF was cloned by PCR on total cDNA extracted from *S. moellendorffii* (purchased from http://www.xplant.co.kr, Seoul). CDS of *SmSMXL* was identified by sequencing with gene-specific primers (F: 5′- ATGCGGGCGGGGGTGTCCAC-3′, R: 5′-GACACCCGTTCGCCTTTGTGGAG-3′). The sequence was aligned to *S. moellendorffii* public genome to correct SNPs. Revised CDS of *SmSMXL* was translated into protein sequence for BLAST analysis. The location of *SmSMXL* is GL377569: 293451-296918 (EnsemblPlant).

Histological analysis. For observation using light microscopy, 6-week-old stem samples were fixed for 3 h in 3% glutaraldehyde in a 0.1 M sodium phosphate buffer (pH 7.2) then rinsed twice with 0.1 M sodium phosphate buffer (pH 7.2), before being dehydrated through a graded acetone series at room temperature. The specimens were infiltrated and embedded in Spurr's resin (Electron Microscopy Sciences) for 48 h at 65 °C. Sections (2 µm) were made using a RM2265 microtome (Leica), stained in 0.025% toluidine blue, and photographed using an Axioplan 2 microscope (Carl Zeiss). For native staining, samples were hand-sectioned with a razor blade, stained with 0.05% toluidine blue for 1 min, rinsed in distilled water for 30 s, mounted in 50% glycerol, and observed using an Axioplan 2 microscope. For transmission electron microscopic observation, fixed tissues were subjected to OsO_4 prior to dehydration.

Histochemical staining. GUS staining assay was carried out as described by previously[69]. Images of GUS-stained tissues were taken using a digital camera mounted on an Axioplan 2 microscope or Stemi SV 11 Apo stereoscope (Carl Zeiss).

Quantitative RT–PCR. Total RNA from inflorescence stems of 6-week old plants was isolated using TRIzol reagent (Invitrogen), following the manufacturer's instructions. Reverse transcription was carried out using 1 µg total RNA, oligo(dT) primers and ImProm-II reverse transcriptase (Promega). qRT–PCR was performed following the instructions provided for the LightCycler 2.0 (Roche Life Science) with the SYBR Premix ExTaq system (Takara Bio). PCR primer sequences are listed in Supplementary Table 4.

Recombinant protein purification. For the purification of GST-fused recombinant proteins, GST-fused JUL1, JUL2, JUL1^{R20A}, JUL1^{R80A}, JUL1^{R146A} JUL1$^{R20/80A}$, JUL1$^{R80/146A}$, JUL1$^{R20/146A}$ or JUL1$^{R20/80/146A}$ were expressed in *Escherichia coli* BL21. The bacterial cells were grown in 200 ml of Luria broth medium at 37 °C until they reached an optical density at 600 nm of 0.8, then further incubated with 0.5 mM IPTG (isopropyl β-d-1-thiogalactopyranoide) for 3 h. The recombinant GST-tagged proteins were purified according to the manufacturer's protocol (GE Healthcare).

SELEX analysis. For the aptamer selection, a library of random-sequence 30-nucleotide synthetic ssDNAs was designed, with each flanked by two primer regions for in vitro transcription and amplification (5′-GATAATACGACTCACTATAGGGTTACCTAGGTGTAGATGCT-$(N)_{30}$- AAGTGACGTCTGAACTGCTTCGAA-3′; T7 promoter underlined) (PMID: 25689224). All DNA oligos were synthesized by Cosmo Genetech (Korea). The ssDNA library was amplified using *i*-pfu, a forward primer (5′-GATAATACGACTCACTATAGGGTTACCTAGGTGTAGATGCT-3′) and a reverse primer (5′-TTCGAAGCAG TTCAGACGTCACTT-3′). The amplification cycle was optimized via gel analysis, and the amplified dsDNA library was purified using a PCR purification kit (Qiagen). The resulting dsDNA library was transcribed using an AmpliScribe T7 High Yield Transcription Kit (Epicentre) at 37 °C for 2 h, then DNase I was used to digest the DNA. The RNA library was purified using a phenol-chloroform-isoamyl alcohol extraction, followed by ethanol precipitation, and the concentration was determined using a NanoDrop 2000 (Thermo Scientific). Before the incubation of the library with the target proteins, the RNA pools were refolded in a binding buffer (20 mM HEPES (pH 7.4), 150 mM KCl and 5 mM $MgCl_2$) by heating at 80 °C for 5 min and slowly cooling to room temperature. The target protein, fused with GST, was immobilized on Pierce Glutathione Magnetic Agarose Beads (Thermo Scientific) in an equilibration buffer (125 mM Tris-HCl, 150 mM KCl, 1 mM DTT, 1 mM EDTA (pH 7.4)). After washing several times with binding buffer, the RNA library was incubated with the target protein-immobilized beads on a slow rocker for 1 h at room temperature. To determine the binding proportion of the RNA library, the amount of unbound RNA was quantified using a NanoDrop. The beads were washed twice with 100 µl of washing buffer and the bound RNA library was eluted in 8 M urea by heating them at 95 °C for 10 min. The eluted RNA pools were recovered via ethanol precipitation, and then reverse transcribed using GoScript Reverse Transcription System (Promega). The resulting oligos were used for the next round of SELEX. Each selection round was repeated using the same procedure described above. After the third round, the RNA pools were incubated with Pierce Glutathione Magnetic Agarose Beads without the immobilized target protein for the negative selection. During the selections, several parameters were altered and stringently controlled: the ratio of RNA to protein increased from 0.5 to 2.5; the incubation time decreased from 1 h to 30 min; the washing volume increased from 100 µl to 200 µl; and the number of washes was increased from two to four. Separate SELEX was performed for native JUL1 and was carried out for up to 15 rounds. The selected RNA pools were amplified by PCR using the forward and reverse primers, and were then cloned into the pENTR/TOPO vector. *Escherichia coli* TOP10 cells (TOPO-TA Cloning Kit; Thermo Fisher Scientific) were transformed with these constructs. The clones containing the ssDNAs were purified using a Miniprep Kit (GeneAll, Korea) and sequenced (Cosmo Genetech). To analyse the structural similarity of the selected RNAs, their secondary structures were investigated using the QGRS program (http://bioinformatics.ramapo.edu/QGRS/index.php).

Electrophoretic mobility shift assay. For the RNA EMSA of the pentaprobe library, single-stranded RNA PPs were produced by linearizing the pcDNA3.1 plasmid with ApaI and filling the resulting 3′ overhang with the DNA polymerase I large (Klenow) fragment (New England Biolabs). Transcription was carried out using the RiboMAX Large Scale RNA Production System-T7 (Promega) in the presence of [α-^{32}P]-UTP (10 mCi ml^{-1}) and the RNA probes were gel purified by denaturing them by gel electrophoresis using a 6% urea-TBE gel. For the RNA EMSA with the *SMXL5* 5′ UTRs, ssRNA oligonucleotides of the *SMXL5* 5′ UTR G-quadruplex-forming regions and the SELEX probes were synthesized. The ssRNA probes were labelled with [γ−^{32}P]-ATP (10 mCi ml^{-1}) by incubating them with T4 polynucleotide kinase (New England Biolabs) for 30 min at 37 °C. The unlabelled radionucleotides were removed using a Illustra MicroSpin G25 column (Amersham). The GST, GST–JUL1, GST–JUL2, GST–JUL1^{R20A}, GST–JUL1^{R80A}, GST–JUL1^{R146A}, GST–JUL1$^{R20/80A}$, GST–JUL1$^{R80/146A}$, GST–JUL1$^{R20/146A}$ or GST–JUL1$^{R20/80/146A}$ proteins were incubated in binding buffer (10 mM Tris-HCl (pH 8.0), 2.5% glycerol, 0.5 mM DTT, 50 µg ml^{-1} BSA, 100 mM KCl, 250 µM EDTA and 1 µg heparin) with 20,000 c.p.m. of ssRNA probes for 20 min in room temperature. The reaction mixture was resolved on a 6% polyacrylamide gel in 0.5× TBE buffer. Gels were visualized on a Phosphor screen using a Typhoon FLA 9000 PhosphorImager (GE Healthcare).

Circular dichroism assay. All CD spectra were obtained from a J-815 Spectropolarimeter (Jasco) at 25 °C using quartz cuvettes with a 2.0 mm path length. Each spectrum was recorded over a wavelength range of 220 nm to 320 nm with a 50 nm min^{-1} scanning speed. The final spectrum encompassed the average of five scans of the same sample. Synthesized RNA oligonucleotides (5 µM) were folded into their G-quadruplex form by slowly cooling them from 95 °C to room temperature in a binding buffer (10 mM Tris-HCl (pH 8.0) and 1 mM $MgCl_2$, either in the absence or presence of 100 mM KCl), and allowed to reach equilibrium prior to CD measurements. The re-natured *SMXL5* 5′ UTR containing the 100 mM KCl was combined with 2.5 µM JUL1 protein and incubated for 30 min before the CD measurement to observe the G-quadruplex structure of the RNA in the *SMXL5*:JUL1 complex. To eliminate the influence of proteins and buffers, the spectra containing the JUL1 protein were corrected using 2.5 µM JUL1 in buffer as a baseline. The spectra of 2.5 µM JUL1 alone were also recorded to demonstrate that JUL1 has no significant effect on the spectrum of the RNA G-quadruplex.

RNA immunoprecipitation. For monitoring the interaction between *SMXL5* 5′ UTR and JUL1, *SMXL5* 5′ UTR–*GFP* was co-transfected into protoplasts with or without *JUL1-HA*. RNA-protein complexes in protoplast lysates were extracted using IP buffer (100 mM KCl, 2.5 mM $MgCl_2$, 10 mM Tris-HCl (pH 8.0), 10% glycerol, 0.5% NP-40, 1 mM DTT, 100 U ml^{-1} RNasin RNase inhibitor (Promega), 25 mM MG132 and a protease inhibitor cocktail for plant cell extraction (Sigma-Aldrich). After removing the insoluble debris by centrifugation at 13,000*g* for 10 min at 4 °C, 300 µl cell extracts were incubated with 1 µg of HA antibody (Roche) for 2 h on ice with occasional gentle mixing. A 30 µl aliquot of the cell extracts was stored at −80 °C for later experiments. Protein G agarose magnetic beads (Bio-Rad Laboratories) were washed three times in washing buffer (100 mM KCl, 2.5 mM $MgCl_2$, 10 mM Tris-HCl (pH 8.0), 10% glycerol, 0.5% NP-40 and 100 U ml^{-1} RNasin RNase inhibitor), then the anti-HA-decorated extracts were incubated with 10 µl protein G agarose magnetic beads for 2 h at 4 °C with constant rotation. The beads were then washed eight times with 1 ml washing buffer. After elution by TRIzol reagent, the co-immunoprecipitated RNA and protein was analysed by qRT–PCR and detected using a horseradish peroxidase (HRP)-conjugated high-affinity anti-HA antibody.

Bead surface interaction assay. For visualizing the RNA G-quadruplex and JUL1 interaction, 20 µl of 5 µM RNA probes were heated for 5 min at 95 °C in structure buffer (10 mM Tris-HCl (pH 8.0), 100 mM KCl, either 100 mM NaCl or 100 mM LiCl, and 1 mM $MgCl_2$), then gradually cooled to 25 °C for 1–2 h. Glutathione-sepharose 4B beads (GE Healthcare) were washed twice with structure buffer and incubated with GST–JUL1 and GST–JUL1$^{R20/80/146A}$ (1.0–2.5 µM) for 1 h at 4 °C. The protein-bead complexes were washed twice with structure buffer and their volume was increased to 20 µl. The cooled, structured RNA probes were added to protein-bead complexes and incubated for 10 min with occasional mixing. ThT or NMM was added to RNA probe-protein-bead complexes to a final concentration of 4 µM. To visualize the G-quadruplex structure bound at the bead surface, the fluorescence of ThT and NMM on the bead surface was observed using a CFP filter (460–500 nm) and an RFP filter (630–690 nm), respectively.

Transient expression in HEK293T cell. HEK293T cells were maintained in Dulbecco's Modified Eagle Medium (Welgene) with 10% foetal bovine serum (FBS), at 37 °C and in a humid atmosphere containing 5% CO_2. Trypsin was used to separate the HEK293T cells during their subculturing. Plasmid transfection was conducted using Metafectene Pro (Biontex Laboratories), according to the manufacturer's instructions. The cells were co-transfected with *JUL1* expression plasmids (either 500 ng or 1,000 ng of the *pCMV10–JUL1* or *pCMV10–JUL1$^{R20/80/146A}$* vectors) and *GFP* reporters (1 µg of *pCMV10–SMXL5* 5′ UTR–*GFP* or *pCMV10–mSMXL5* 5′ UTR–*GFP*). Forty-eight hours after transfection, the cells were harvested and subjected to western blot analysis.

Sucrose density gradient analysis. Polysome profiles were obtained from Col-0, *JUL1/2* RNAi seedlings and *Arabidopsis* protoplasts expressing *SMXL5* 5′ UTR–*GFP* in the absence or presence of *JUL-HA*. Briefly, the cells were treated with 100 µg ml^{-1} cycloheximide for 30 min and were lysed in polysome lysis buffer (200 mM Tris-HCl (pH 8.0), 50 mM KCl, 25 mM $MgCl_2$, 0.1 mM DTT, 0.5% NP-40, and 100 µg ml^{-1} cycloheximide). For each sample, 250 µl cell extract was resolved on 5–45% sucrose gradients in polysome buffer (200 mM Tris-HCl (pH 8.0), 50 mM KCl, 25 mM $MgCl_2$ and 0.1 mM DTT) using ultracentrifugation for 3 h at 30,000 r.p.m. in a SW41Ti rotor (Beckman Coulter). A 0.25 ml fraction aliquot was obtained via a gradient density fractionator (Brandel), using upward displacement with 60% (w/v) sucrose at a flow rate of 0.5 ml min^{-1}. Continuous monitoring was performed at an absorbance of 254 nm using an Econo UV monitor (Bio-Rad Laboratories). Total RNA of each fraction was isolated using TRIzol reagent, subjected to qRT–PCR, and *GFP* or *TUB4* mRNA transcript level in each fraction was normalized by total input mRNA level of *GFP* or *TUB4*.

Analysis of yield component traits. Average seed mass was determined by weighing 100 mature dry seeds of *Arabidopsis* and tobacco. The weights of at least three samples were measured for each seed lot.

Measurement of the dissociation constant using a fluorescence assay. The equilibrium dissociation constants were measured using a standard fluorescence assay[70]. All RNA samples were re-natured in binding buffer by heated them to 95 °C for 5 min then slowly cooling them to room temperature for 1 h prior to use. Fluorescein (FAM)-modified RNA samples were diluted to various concentrations from 0 nM to 500 nM in 100 µl binding buffer, then mixed with JUL1-immobilized magnetic beads. The mixtures were incubated in the dark with light shaking at room temperature for 1 h. After washing, the unbound RNA twice using the binding buffer, the RNA–JUL1 complexes were eluted twice with 100 µl binding buffer supplemented with 500 mM imidazole. The fluorescence intensity of

the elutants was measured using a 528/20 nm emission filter (with 485/20 nm excitation filter) on a Synergy HT multi-detection microplate reader (BioTek). K_d values were calculated by fitting them to a kinetic model, the 'exponential decay 1' model of OriginPro 9.0 software (OriginLab).

Confocal analysis. For the co-localization analysis of the MS2 protein, the MS2 hairpin-fused *SMXL5* 5′ UTR and the JUL1 protein, GFP and mRFP fluorescences were visualized under a confocal microscope (LSM510, Carl Zeiss). GFP was excited using the 488 nm wavelength argon laser lines. mRFP was excited using the 543 nm wavelength HeNe laser line. Emission wavelengths between 500 nm and 520 nm were recorded for the GFP fluorescence and between 580 nm and 645 nm for mRFP fluorescence. For the co-localization of GFP and mRFP, reconstructed Z-stack series were rendered as 3D interactive graphics. For the cytosolic accumulation of JUL1 protein, the samples were treated with 0.01% NaN_3 was treated for 10 min. For ThT fluorescence detection in protoplasts, 10 µM ThT was applied to the sample for 10 min before being excited with the 405 nm wavelength argon laser, with emission wavelengths between 450 nm and 490 nm being collected. The imaging of YFP-expressing roots was achieved by exciting the sample using an argon laser at 514 nm and detecting the emissions at a wavelength range of 520–540 nm.

CFDA treatment and measurement. A 5 µM sample of CFDA-SE (Thermo Fisher) was directly applied to seedlings that were 1.5 cm long (selected from 4-day-old seedlings) through cotyledon after cutting. After CFDA treatment, seedlings were placed on 5% agarose gel to prevent drying. CFDA fluorescence in the root tip was observed by a fluorescence microscope (Axioplan 2) by GFP filter at 0, 2 and 3 min after CFDA treatment. Fluorescence intensities were quantified by imageJ.

Reverse transcriptase stalling assay. In vitro RT-stop assay was adopted with few modifications from the previous study[36]. RNA Templates for in vitro RT-stop assay were prepared using pre-annealed DNA containing minimal T7 promoter. After in vitro transcription using RiboMAXTM Large Scale RNA production system-T7 (Promega), products were purified by PCI/CI purification and subjected into gel-filtration using G25 column (GE healthcare). A 150–200 µg sample of the template was added up to 8 µl with nuclease-free water, 1 µl of 5 µM radio-labelled primer, in the absence or presence of 1 µl of 10 µM of pyridostatin (PDS) to final concentration of 100 mM of LiCl, NaCl, or KCl. The mixtures were pre-incubated at 25 °C for 20 min and then heated at 70 °C for 3 min, and incubated at 4 °C for 10 min for primer annealing to template. RT reaction was performed as manufactures instruction (Super-script IV; Invitrogen) with 150 mM of LiCl, NaCl or KCl condition. The final mixture was incubated at 25 °C for 10 min, followed by 50 °C for 20 min for reverse transcription. To stop the RT reaction, 1 µl of 1 N NaOH. Denaturing buffer (2× formamide) was added, incubated at 95 °C for 2 min and subsequently cooled on ice. RT products were separated on 8 M UREA denaturing gel, fixed by 20% ethanol, 5% acetic acid, and visualized by a Phosphor screen using a Typhoon FLA 9000 PhosphorImager (GE Healthcare).

Reporting Summary. Further information on experimental design is available in the Nature Research Reporting Summary linked to this article.

Data availability. The data that support the findings of this study are available from the corresponding author upon request.

Received: 9 November 2017; Accepted: 19 April 2018;
Published online: 28 May 2018

References

1. Heo, J. O., Roszak, P., Furuta, K. M. & Helariutta, Y. Phloem development: current knowledge and future perspectives. *Am. J. Bot.* **101**, 1393–1402 (2014).
2. Lucas, W. J. et al. The plant vascular system: evolution, development and functions. *J. Integr. Plant Biol.* **55**, 294–388 (2013).
3. Thompson, G. A. & van Bel, A. J. E. *Phloem: Molecular Cell Biology, Systemic Communication, Biotic Interactions*. (John Wiley & Sons, Oxford, 2012).
4. Cronk, Q. C. Plant evolution and development in a post-genomic context. *Nat. Rev. Genet.* **2**, 607–619 (2001).
5. Sanderson, M. J., Thorne, J. L., Wikstrom, N. & Bremer, K. Molecular evidence on plant divergence times. *Am. J. Bot.* **91**, 1656–1665 (2004).
6. De Rybel, B., Mahonen, A. P., Helariutta, Y. & Weijers, D. Plant vascular development: from early specification to differentiation. *Nat. Rev. Mol. Cell Biol.* **17**, 30–40 (2016).
7. Furuta, K. M. et al. Plant development. *Arabidopsis* NAC45/86 direct sieve element morphogenesis culminating in enucleation. *Science* **345**, 933–937 (2014).
8. Rodriguez-Villalon, A. et al. Molecular genetic framework for protophloem formation. *Proc. Natl Acad. Sci. USA* **111**, 11551–11556 (2014).
9. Castello, A. et al. Insights into RNA biology from an atlas of mammalian mRNA-binding proteins. *Cell* **149**, 1393–1406 (2012).
10. Kwon, S. C. et al. The RNA-binding protein repertoire of embryonic stem cells. *Nat. Struct. Mol. Biol.* **20**, 1122–1130 (2013).
11. Ye, J. & Blelloch, R. Regulation of pluripotency by RNA binding proteins. *Cell Stem Cell* **15**, 271–280 (2014).
12. Young, R. A. Control of the embryonic stem cell state. *Cell* **144**, 940–954 (2011).
13. Incarnato, D. & Oliviero, S. The RNA epistructurome: uncovering RNA function by studying structure and post-transcriptional modifications. *Trends Biotechnol.* **35**, 318–333 (2017).
14. Lewis, C. J., Pan, T. & Kalsotra, A. RNA modifications and structures cooperate to guide RNA-protein interactions. *Nat. Rev. Mol. Cell Biol.* **18**, 202–210 (2017).
15. Lu, Z. & Chang, H. Y. Decoding the RNA structurome. *Curr. Opin. Struct. Biol.* **36**, 142–148 (2016).
16. Mortimer, S. A., Kidwell, M. A. & Doudna, J. A. Insights into RNA structure and function from genome-wide studies. *Nat. Rev. Genet.* **15**, 469–479 (2014).
17. Vandivier, L. E., Anderson, S. J., Foley, S. W. & Gregory, B. D. The conservation and function of RNA secondary structure in plants. *Annu. Rev. Plant Biol.* **67**, 463–488 (2016).
18. Schrader, J. et al. A high-resolution transcript profile across the wood-forming meristem of poplar identifies potential regulators of cambial stem cell identity. *Plant Cell* **16**, 2278–2292 (2004).
19. Zhao, C. S., Craig, J. C., Petzold, H. E., Dickerman, A. W. & Beers, E. P. The xylem and phloem transcriptomes from secondary tissues of the Arabidopsis root-hypocotyl. *Plant Physiol.* **138**, 803–818 (2005).
20. Gonzali, S. et al. Identification of sugar-modulated genes and evidence for in vivo sugar sensing in *Arabidopsis*. *J. Plant Res.* **119**, 115–123 (2006).
21. Senthil-Kumar, M. & Mysore, K. S. Tobacco rattle virus-based virus-induced gene silencing in *Nicotiana benthamiana*. *Nat. Protoc.* **9**, 1549–1562 (2014).
22. Kondo, Y. et al. Vascular cell induction culture system using *Arabidopsis* leaves (VISUAL) reveals the sequential differentiation of sieve element-like cells. *Plant Cell* **28**, 1250–1262 (2016).
23. Froelich, D. R. et al. Phloem ultrastructure and pressure flow: sieve-element-occlusion-related agglomerations do not affect translocation. *Plant Cell* **23**, 4428–4445 (2011).
24. Loughlin, F. E. et al. The zinc fingers of the SR-like protein ZRANB2 are single-stranded RNA-binding domains that recognize 5′ splice site-like sequences. *Proc. Natl Acad. Sci. USA* **106**, 5581–5586 (2009).
25. Nguyen, C. D. et al. Characterization of a family of RanBP2-type zinc fingers that can recognize single-stranded RNA. *J. Mol. Biol.* **407**, 273–283 (2011).
26. Bendak, K. et al. A rapid method for assessing the RNA-binding potential of a protein. *Nucleic Acids Res.* **40**, e105 (2012).
27. Ellington, A. D. & Szostak, J. W. In vitro selection of RNA molecules that bind specific ligands. *Nature* **346**, 818–822 (1990).
28. Tuerk, C. & Gold, L. Systematic evolution of ligands by exponential enrichment: RNA ligands to bacteriophage T4 DNA polymerase. *Science* **249**, 505–510 (1990).
29. Neidle, S. & Balasubramanian, S. *Quadruplex Nucleic Acids*. (RSC Pub., Cambridge, 2006).
30. Mullen, M. A. et al. RNA G-Quadruplexes in the model plant species *Arabidopsis thaliana*: prevalence and possible functional roles. *Nucleic Acids Res* **38**, 8149–8163 (2010).
31. Wallner, E. S. et al. Strigolactone- and Karrikin-independent SMXL proteins are central regulators of phloem formation. *Curr. Biol.* **27**, 1241–1247 (2017).
32. Kikin, O., D'Antonio, L. & Bagga, P. S. QGRS mapper: a web-based server for predicting G-quadruplexes in nucleotide sequences. *Nucleic Acids Res.* **34**, W676–W682 (2006).
33. Renaud de la Faverie, A., Guedin, A., Bedrat, A., Yatsunyk, L. A. & Mergny, J. L. Thioflavin T as a fluorescence light-up probe for G4 formation. *Nucleic Acids Res.* **42**, e65 (2014).
34. Xu, S. et al. Thioflavin T as an efficient fluorescence sensor for selective recognition of RNA G-quadruplexes. *Sci. Rep.* **6**, 24793 (2016).
35. Kreig, A. et al. G-quadruplex formation in double strand DNA probed by NMM and CV fluorescence. *Nucleic Acids Res.* **43**, 7961–7970 (2015).
36. Kwok, C. K. & Balasubramanian, S. Targeted detection of G-quadruplexes in cellular RNAs. *Angew. Chem. Int. Ed.* **54**, 6751–6754 (2015).
37. Biffi, G., Tannahill, D., McCafferty, J. & Balasubramanian, S. Quantitative visualization of DNA G-quadruplex structures in human cells. *Nat. Chem.* **5**, 182 (2013).
38. Bertrand, E. et al. Localization of ASH1 mRNA particles in living yeast. *Mol. Cell* **2**, 437–445 (1998).
39. Bugaut, A. & Balasubramanian, S. 5′-UTR RNA G-quadruplexes: translation regulation and targeting. *Nucleic Acids Res.* **40**, 4727–4741 (2012).
40. Oparka, K. J., Duckett, C. M., Prior, D. A. M. & Fisher, D. B. Real-time imaging of phloem unloading in the root tip of *Arabidopsis*. *Plant J.* **6**, 759–766 (1994).

41. Nieminen, K., Blomster, T., Helariutta, Y. & Mahonen, A. P. Vascular cambium development. *Arabidopsis Book* **13**, e0177 (2015).
42. Ruan, Y. L. Sucrose metabolism: gateway to diverse carbon use and sugar signaling. *Annu Rev. Plant Biol.* **65**, 33–67 (2014).
43. Vreugdenhil, D. Source-to-sink gradient of potassium in the phloem. *Planta* **163**, 238–240 (1985).
44. Bihmidine, S., Hunter, C. T. 3rd, Johns, C. E., Koch, K. E. & Braun, D. M. Regulation of assimilate import into sink organs: update on molecular drivers of sink strength. *Front. Plant Sci.* **4**, 177 (2013).
45. Braun, D. M., Wang, L. & Ruan, Y. L. Understanding and manipulating sucrose phloem loading, unloading, metabolism, and signalling to enhance crop yield and food security. *J. Exp. Bot.* **65**, 1713–1735 (2014).
46. Yu, S. M., Lo, S. F. & Ho, T. H. Source-sink communication: regulated by hormone, nutrient, and stress cross-signaling. *Trends Plant Sci.* **20**, 844–857 (2015).
47. Gellert, M., Lipsett, M. N. & Davies, D. R. Helix formation by guanylic acid. *Proc. Natl Acad. Sci. USA* **48**, 2013–2018 (1962).
48. Kwok, C. K., Ding, Y., Shahid, S., Assmann, S. M. & Bevilacqua, P. C. A stable RNA G-quadruplex within the 5′-UTR of *Arabidopsis thaliana* ATR mRNA inhibits translation. *Biochem. J.* **467**, 91–102 (2015).
49. Brown, V. et al. Microarray identification of FMRP-associated brain mRNAs and altered mRNA translational profiles in fragile X syndrome. *Cell* **107**, 477–487 (2001).
50. Darnell, J. C. et al. Fragile X mental retardation protein targets G quartet mRNAs important for neuronal function. *Cell* **107**, 489–499 (2001).
51. Napoli, I. et al. The fragile X syndrome protein represses activity-dependent translation through CYFIP1, a new 4E-BP. *Cell* **134**, 1042–1054 (2008).
52. Wolfe, A. L. et al. RNA G-quadruplexes cause eIF4A-dependent oncogene translation in cancer. *Nature* **513**, 65–70 (2014).
53. Guo, J. U. & Bartel, D. P. RNA G-quadruplexes are globally unfolded in eukaryotic cells and depleted in bacteria. *Science* **353**, aaf5371 (2016).
54. Fay, M. M., Lyons, S. M. & Ivanov, P. RNA G-quadruplexes in biology: principles and molecular mechanisms. *J. Mol. Biol.* **429**, 2127–2147 (2017).
55. Halder, K., Wieland, M. & Hartig, J. S. Predictable suppression of gene expression by 5′-UTR-based RNA quadruplexes. *Nucleic Acids Res.* **37**, 6811–6817 (2009).
56. Brady, S. M. et al. A high-resolution root spatiotemporal map reveals dominant expression patterns. *Science* **318**, 801–806 (2007).
57. Depuydt, S. et al. Suppression of *Arabidopsis* protophloem differentiation and root meristem growth by CLE45 requires the receptor-like kinase BAM3. *Proc. Natl Acad. Sci. USA* **110**, 7074–7079 (2013).
58. Guo, Y., Qin, G., Gu, H. & Qu, L. J. Dof5.6/HCA2, a Dof transcription factor gene, regulates interfascicular cambium formation and vascular tissue development in Arabidopsis. *Plant Cell* **21**, 3518–3534 (2009).
59. Takahama, K., Takada, A., Tada, S., Shimizu, M., Sayama, K., Kurokawa, R. & Oyoshi, T. Regulation of telomere length by G-quadruplex telomere DNA-and TERRA-binding protein TLS/FUS. *Chem. & Biol.* **20**, 341–350 (2013).
60. Karimi, M., Inze, D. & Depicker, A. GATEWAY vectors for *Agrobacterium*-mediated plant transformation. *Trends Plant Sci.* **7**, 193–195 (2002).
61. Chen, S., Songkumarn, P., Liu, J. & Wang, G. L. A versatile zero background T-vector system for gene cloning and functional genomics. *Plant Physiol.* **150**, 1111–1121 (2009).
62. Hwang, I. & Sheen, J. Two-component circuitry in *Arabidopsis* cytokinin signal transduction. *Nature* **413**, 383–389 (2001).
63. Clough, S. J. & Bent, A. F. Floral dip: a simplified method for *Agrobacterium*-mediated transformation of *Arabidopsis thaliana*. *Plant J.* **16**, 735–743 (1998).
64. Sievers, F. et al. Fast, scalable generation of high-quality protein multiple sequence alignments using Clustal Omega. *Mol. Syst. Biol.* **7**, 539 (2011).
65. Yamada, K. D., Tomii, K. & Katoh, K. Application of the MAFFT sequence alignment program to large data-reexamination of the usefulness of chained guide trees. *Bioinformatics* **32**, 3246–3251 (2016).
66. Capella-Gutierrez, S., Silla-Martinez, J. M. & Gabaldon, T. trimAl: a tool for automated alignment trimming in large-scale phylogenetic analyses. *Bioinformatics* **25**, 1972–1973 (2009).
67. Minh, B. Q., Nguyen, M. A. & von Haeseler, A. Ultrafast approximation for phylogenetic bootstrap. *Mol. Biol. Evol.* **30**, 1188–1195 (2013).
68. Trifinopoulos, J., Nguyen, L. T., von Haeseler, A. & Minh, B. Q. W-IQ-TREE: a fast online phylogenetic tool for maximum likelihood analysis. *Nucleic Acids Res.* **44**, W232–W235 (2016).
69. Millar, A. A. & Gubler, F. The *Arabidopsis* GAMYB-like genes, MYB33 and MYB65, are microRNA-regulated genes that redundantly facilitate anther development. *Plant Cell* **17**, 705–721 (2005).
70. Cho, M. et al. Quantitative selection of DNA aptamers through microfluidic selection and high-throughput sequencing. *Proc. Natl Acad. Sci. USA* **107**, 15373–15378 (2010).

Acknowledgements

We thank V.N. Kim for critical reading and useful suggestions, H.S. Yoon for advice on phylogenetic analysis. This work was supported by grants to I.H. from the Basic Science Research Programme (2017R1A2A1A17069734) through the National Research Foundation (NRF) funded by the Ministry of Science, ICT and Future Planning, and from the Cooperative Research Programme for Agriculture Science & Technology Development (PJ010953022018) funded by Rural Development Administration, Korea. T.V.T.D is supported by the Korean Research Fellowship programme (2017H1D3A1A03055171).

Author contributions

H.C. and H.S.C. performed all experiments. H.C. and I.H. designed the experiments and analysed data. J.Y. performed genetic screening for charactering JUL. H.J. performed the RNA SELEX analysis and analysed data with H.C. and C.B. C.P. performed phylogenetic analysis. T.V.T.D. conducted reporter assay using protoplast. H.N. contributed to VISUAL analysis. H.Y. performed CD analysis. J.Jeon conducted dissociation constant measurement. E.K. performed sucrose density gradient analysis with S.K.J. J.P. conducted reporter assay with HEK293T cell with Y.L. H.C. and I.H. wrote the manuscript.

Competing interests

The authors declare no competing interests.

Additional information

Supplementary information is available for this paper at https://doi.org/10.1038/s41477-018-0157-2.

Reprints and permissions information is available at www.nature.com/reprints.

Correspondence and requests for materials should be addressed to I.H.

Publisher's note: Springer Nature remains neutral with regard to jurisdictional claims in published maps and institutional affiliations.

nature research

Corresponding author(s): Ildoo Hwang

☐ Initial submission ☐ Revised version ☒ Final submission

Life Sciences Reporting Summary

Nature Research wishes to improve the reproducibility of the work that we publish. This form is intended for publication with all accepted life science papers and provides structure for consistency and transparency in reporting. Every life science submission will use this form; some list items might not apply to an individual manuscript, but all fields must be completed for clarity.

For further information on the points included in this form, see Reporting Life Sciences Research. For further information on Nature Research policies, including our data availability policy, see Authors & Referees and the Editorial Policy Checklist.

Experimental design

1. Sample size

Describe how sample size was determined.

No statistical methods were used to determine sample size. Sample size was determined to be adequate based on the magnitude and consistency of measurable differences between groups.

2. Data exclusions

Describe any data exclusions.

No data points were excluded from analysis in any experiment depicted in this manuscript.

3. Replication

Describe whether the experimental findings were reliably reproduced.

For each series of the experiments, all attempts at replication were successful.

4. Randomization

Describe how samples/organisms/participants were allocated into experimental groups.

Plants were assigned randomly to experimental and control groups.

5. Blinding

Describe whether the investigators were blinded to group allocation during data collection and/or analysis.

The investigators were blinded to group allocation during data collection and analysis.

Note: all studies involving animals and/or human research participants must disclose whether blinding and randomization were used.

6. Statistical parameters

For all figures and tables that use statistical methods, confirm that the following items are present in relevant figure legends (or in the Methods section if additional space is needed).

n/a	Confirmed
☐	☒ The exact sample size (*n*) for each experimental group/condition, given as a discrete number and unit of measurement (animals, litters, cultures, etc.)
☐	☒ A description of how samples were collected, noting whether measurements were taken from distinct samples or whether the same sample was measured repeatedly
☐	☒ A statement indicating how many times each experiment was replicated
☐	☒ The statistical test(s) used and whether they are one- or two-sided (note: only common tests should be described solely by name; more complex techniques should be described in the Methods section)
☐	☒ A description of any assumptions or corrections, such as an adjustment for multiple comparisons
☐	☒ The test results (e.g. *P* values) given as exact values whenever possible and with confidence intervals noted
☐	☒ A clear description of statistics including central tendency (e.g. median, mean) and variation (e.g. standard deviation, interquartile range)
☐	☒ Clearly defined error bars

See the web collection on statistics for biologists for further resources and guidance.

Software

Policy information about availability of computer code

7. Software

Describe the software used to analyze the data in this study.	R (v3.0.1), ClustalO, MAFFT, TrimAl, QGRS mapper, BLAST

For manuscripts utilizing custom algorithms or software that are central to the paper but not yet described in the published literature, software must be made available to editors and reviewers upon request. We strongly encourage code deposition in a community repository (e.g. GitHub). *Nature Methods* guidance for providing algorithms and software for publication provides further information on this topic.

Materials and reagents

Policy information about availability of materials

8. Materials availability

Indicate whether there are restrictions on availability of unique materials or if these materials are only available for distribution by a for-profit company.	Every material we used is readily available form standard commercial sources

9. Antibodies

Describe the antibodies used and how they were validated for use in the system under study (i.e. assay and species).	1. Rat anti-HA peroxidase, high-affinity from rat IgG, Cat no: 12013819001, clone3F10, monoclonal, ROCHE. https://www.sigmaaldrich.com/catalog/product/roche/12013819001 Reference for validation of this antibody: PMID 24782309 2. GFP (B-2) HRP, Cat no: sc-9996 HRP, clone B-2, monoclonal, Santa cruz biotechnology, Inc. https://www.scbt.com/scbt/ko/product/gfp-antibody-b-2 Reference for validation of this antibody: PMID: 28419207

10. Eukaryotic cell lines

a. State the source of each eukaryotic cell line used.	HEK293T (ATCC® CRL-3216™)
b. Describe the method of cell line authentication used.	HEK293FT cells were functionally authenticated by positive selection for pCMV10 expression
c. Report whether the cell lines were tested for mycoplasma contamination.	Cell lines tested negative for mycoplasma contamination
d. If any of the cell lines used are listed in the database of commonly misidentified cell lines maintained by ICLAC, provide a scientific rationale for their use.	No commonly misidentified cell lines were used

Animals and human research participants

Policy information about studies involving animals; when reporting animal research, follow the ARRIVE guidelines

11. Description of research animals

Provide details on animals and/or animal-derived materials used in the study.	The study did not involve animal and/or human research participants.

Policy information about studies involving human research participants

12. Description of human research participants

Describe the covariate-relevant population characteristics of the human research participants.	The study did not involve animal and/or human research participants.